Journal of Alloys and Compounds 1064 (2026) 187968

Contents lists available at ScienceDirect

Journal of Alloys and Compounds

journal homepage: www.elsevier.com/locate/jalcom

Thermoluminescence properties and trap hierarchy of $GdBa_3B_9O_{18}$ revealed by multi-method kinetic analysis

Abeer S. Altowyan [a,*], E.A. Cin [b], M. Oglakci [c], Jabir Hakami [d], M.B. Coban [e,f], U.H. Kaynar [g], N. Can [d,*]

[a] Department of Physics, College of Science, Princess Nourah Bint Abdulrahman University, P.O. Box 84428, Riyadh 11671, Saudi Arabia
[b] Bakircay University, Graduate School of Natural and Applied Sciences, Menemen, Izmir, Türkiye
[c] Physics Department, Cukurova University, Arts-Sciences Faculty, Adana 01330, Türkiye
[d] Jazan University, College of Science, Department of Physical Sciences, Physics Division, P.O. Box 114, Jazan 45142, Saudi Arabia
[e] Balikesir University, Faculty of Arts and Sciences, Department of Physics, Balikesir, Turkiye
[f] Balikesir University, Science and Technology Application and Research Center, Balikesir, Turkiye
[g] Bakircay University, Faculty of Engineering and Architecture, Department of Fundamental Sciences, Menemen, Izmir, Türkiye

ARTICLE INFO

Keywords:
Thermoluminescence
Borate phosphor
Glow curve deconvolution (CGCD)
Trap depth distribution
Charge redistribution

ABSTRACT

This work reports the first thermoluminescence (TL) investigation of trigonal borate phosphor $GdBa_3B_9O_{18}$. The material was synthesized via a urea-assisted sol–gel combustion route and structurally confirmed as a single-phase trigonal borate with space group ($P6_3/m$). The TL response was evaluated under β-irradiation over a dose range of 1.4–500 Gy through dose–response, fading, reusability, and heating-rate experiments combined with a multi-method kinetic analysis. The integrated TL signal exhibits a near-linear power-law dose dependence ($b \approx 1.01$) between 1.4 and 200 Gy, followed by only mild supralinearity up to 500 Gy. A minimum detectable dose of ~0.11 Gy was obtained, indicating potential applicability in medium- to high-dose dosimetry. Reusability tests reveal cycle-to-cycle variations within ±5% over ten irradiation–readout cycles while maintaining a stable glow-curve structure. Heating-rate measurements (0.5–4 °C s^{-1}), combined with the Kitis–Tuyn temperature-lag correction, confirm that the observed glow-peak shifts arise predominantly from intrinsic TL kinetics rather than instrumental artifacts. Variable-heating-rate (VHR), IR–T_m–T_{stop}, and computerized glow-curve deconvolution (CGCD) analyses indicate a hierarchical trap structure with activation energies ranging from ~0.87–1.98 eV and general-order kinetics ($b \approx 1.2$–1.5), consistent with an energetically distributed trap system. Fading measurements reveal an unusual anti-fading behaviour, where the TL intensity reaches a maximum after ~12 h prior to the onset of conventional decay. Extended measurements up to 20 days further confirm that this non-monotonic behavior evolves into a long-term decay regime. This behavior is consistent with time-dependent charge redistribution from shallow to deeper traps via retrapping processes. Overall, these results demonstrate that $GdBa_3B_9O_{18}$ is a structurally stable borate phosphor with robust TL characteristics and promising potential for dosimetric applications in the Gy dose regime.

1. Introduction

Borate-based hosts have emerged as an important class of thermoluminescent (TL) materials due to their relatively low effective atomic number, thermal and chemical stability, and structural adaptability, enabling a tissue-equivalent response and reliable signal readout for medical and environmental dosimetry [1,2]. Classical lithium borates such as $Li_2B_4O_7$ have established borates as viable dosimetric systems, and subsequent research has extended to more complex borate frameworks including $Ca_4LaO(BO_3)_3$, $Ca_4YO(BO_3)_3$, $YAl_3(BO_3)_4$, $GdAl_3(BO_3)_4$, and $Li_3Al_3(BO_3)_4$:Gd [3–10] These materials frequently exhibit linear or quasi-linear dose responses, acceptable reusability, and tunable trapping structures appropriate for both clinical and high-dose applications. Accordingly, their suitability is commonly assessed through dose-response linearity, fading behavior, reusability, and the stability of trap parameters under repeated irradiation–readout cycles. The compositional flexibility of borate networks allows cation substitution (Ca/Y/La/Gd, Li/Al) and rare-earth incorporation to modulate

* Corresponding authors.
E-mail addresses: asaltowyan@pnu.edu.sa (A.S. Altowyan), ncan@jazanu.edu.sa (N. Can).

https://doi.org/10.1016/j.jallcom.2026.187968
Received 7 March 2026; Received in revised form 2 April 2026; Accepted 10 April 2026
Available online 13 April 2026

both trap density and trap energetics, thereby tailoring dosimetric performance [3,9,11–14].

From a mechanistic perspective, dosimetric suitability is governed not solely by the architecture of trapping and recombination centers. The activation energy (trap depth) determines the thermal lifetime of trapped carriers at ambient conditions and thus defines the balance between signal stability and readout temperature. Shallow traps ($<$ ~0.8 eV) typically lead to rapid fading, whereas deeper traps (~1–2 eV) enable long-term retention but require higher stimulation temperatures [15–18]. In addition, kinetic order reflects the degree of retrapping and competition among traps and recombination centers. General-order behavior, commonly resolved in borate phosphors through glow-curve deconvolution, indicates mixed retrapping–recombination pathways and strongly influences peak symmetry, dose linearity, and saturation characteristics [19,20].

Glow-curve stability under variable heating rates, repeated readout, and storage conditions has become a key diagnostic tool for understanding microscopic transport mechanisms. In several borate systems unusual heating-rate dependencies have been reported, where peak intensity increases or deviates from classical thermal-quenching behaviour [3,11,15,16,21]. Such phenomena have been interpreted within semi-localized transition models or kinetic-trapping frameworks involving competition between radiative and non-radiative recombination channels. In parallel, reusability within a few percent over repeated irradiation–readout cycles and controlled fading behavior derived from trap parameters remain essential for reliable dose reconstruction [22–24].

Because different kinetic approaches may yield discrepant activation energies for the same material, contemporary TL analysis increasingly relies on cross-validation using complementary techniques [25,26]. Variable heating rate (VHR), initial rise (IR/T_m–T_{stop}), and computerized glow-curve deconvolution (CGCD) are therefore applied in combination to resolve overlapping peaks, distinguish discrete from continuous trap distributions, and ensure internal consistency of trap depth, frequency factor, and kinetic order [27–29]. Agreement between independent kinetic methods has been shown to strengthen the physical credibility of trap assignments, whereas deviations—particularly under anomalous heating-rate conditions—often indicate semi-localized transition mechanisms. Recent high-dose phosphor studies have further demonstrated that close agreement between IR/ T_m–T_{stop} and deconvolution-derived activation energies enhances the robustness of trap assignment and supports reliable dosimetric application [29]. Consequently, multi-method kinetic validation is fundamental for reliable interpretation of fading, reusability, and dose-response behavior.

Within this expanding borate family, gadolinium-containing hosts have primarily been investigated in aluminate and lithium–aluminum borate matrices, where Gd^{3+} either forms part of the host lattice ($GdAl_3(BO_3)_4$, $GdAlO_3$) or acts as a dopant ($Li_3Al_3(BO_3)_4$:Gd) [3,16,30–32]. These systems have demonstrated promising linear dose ranges, stable response, and complex trap structures resolved via CGCD and multi-method kinetic analysis. Extensive TL investigations have also been reported for related borate systems such as $NaBaBO_3$:Gd^{3+} (3), $LaCa_4O(BO_3)_3$:Tb^{3+}, $Ca_4YO(BO_3)_3$, and various borate glasses and Ba-containing hosts [3,33–35], where detailed glow-curve, trap-depth, and dosimetric analyses have been performed. However, to the best of our knowledge, no TL measurements, glow-curve analyses, or kinetic evaluations have been reported for the trigonal borate $GdBa_3B_9O_{18}$ in the peer-reviewed literature. Notably, $GdBa_3B_9O_{18}$ is not listed among previously reported Gd-containing TL hosts in existing dosimetric surveys, nor has it been discussed in studies addressing anomalous heating-rate behaviour or multi-peak trap structures in borate systems.

Given its distinct cation topology, characterized by Gd–Ba coordination embedded within a rigid B–O framework, systematic evaluation of its TL behaviour is therefore warranted. In contrast to previously studied $GdAl_3(BO_3)_4$ and $Li_3Al_3(BO_3)_4$:Gd systems dominated by Al-centered polyhedral frameworks, $GdBa_3B_9O_{18}$ presents a Ba-rich trigonal lattice with different polyhedral connectivity and charge-compensation environment, potentially leading to a modified trap spectrum, altered retrapping probability, and distinct heating-rate response.

The present work represents the first comprehensive TL investigation of trigonal $GdBa_3B_9O_{18}$. Unlike previously studied $GdAl_3(BO_3)_4$ and $Li_3Al_3(BO_3)_4$:Gd systems dominated by Al-centered polyhedral frameworks, $GdBa_3B_9O_{18}$ incorporates a Ba-rich trigonal lattice with distinct polyhedral connectivity and charge-compensation pathways, which may give rise to modified trap energetics and an altered heating-rate response. Accordingly, this study aims to (i) structurally validate the $GdBa_3B_9O_{18}$ host framework, (ii) characterize its glow-curve features and underlying trap architecture through cross-validated kinetic approaches including IR/T_m–T_{stop}, VHR, and CGCD analyses, (iii) evaluate dose-response linearity, minimum detectable dose, fading, and reusability with respect to dosimetric applicability, and (iv) assess whether the Ba-dominated topology leads to a discrete or energetically distributed trap hierarchy relative to Al-centered borate systems. By integrating structural verification with multi-method kinetic validation, this work aims to clarify how lattice topology influences Gd-centered defect formation, trap hierarchy and dosimetric stability within a previously unexplored borate framework.

2. Experimental procedure

2.1. Preparation of $GdBa_3B_9O_{18}$ phosphors

$GdBa_3B_9O_{18}$ nanopowders were synthesized via a urea-assisted sol–gel combustion method. All chemicals were of analytical grade and were used without further purification. Gadolinium nitrate ($Gd(NO_3)_3{\cdot}xH_2O$), barium nitrate ($Ba(NO_3)_2{\cdot}xH_2O$, Sigma-Aldrich, $\geq$ 99.9%), boric acid (H_3BO_3, Merck), and urea ($CO(NH_2)_2$) were used as starting materials. Stoichiometric amounts of the nitrate salts were dissolved in 20 mL of deionized water in a quartz beaker. Subsequently, H_3BO_3 and urea were added to the solution. The amount of urea was adjusted to maintain a urea-to-nitrate molar ratio of 2.5 during the combustion process. The mixture was magnetically stirred at 80 °C for 1 h under covered conditions to obtain a homogeneous solution and ensure complete dissolution. The cover was then removed, and stirring was continued at the same temperature to evaporate excess water. As evaporation proceeded, the solution became viscous and eventually transformed into a gel. The resulting gel was subjected to microwave-assisted combustion in a household microwave oven. A rapid and vigorous combustion reaction occurred within a short time, accompanied by intense gas evolution, yielding a voluminous, porous white powder. The as-combusted powders were collected and calcined in air at 800 °C for 2 h to remove residual organic species and improve crystallinity. After calcination, the samples were cooled to room temperature and stored in a desiccator until further characterization.

2.2. Characterization techniques

X-ray diffraction (XRD) analyses were performed to investigate the phase purity and structural formation of $GdBa_3B_9O_{18}$. The measurements were conducted using a PANalytical Empyrean diffractometer (Malvern PANalytical) operating with Cu Kα radiation (λ = 1.5406 Å). The diffraction data were collected within a 2θ range of 10°–80°, allowing comprehensive phase identification.

TL characterization was carried out using a Lexsyg Smart TL/OSL reader (Freiberg Instruments, Germany) [36], which is equipped with an integrated $^{90}Sr/^{90}Y$ β source delivering a nominal dose rate of approximately 1.436 Gy s^{-1} . All experimental procedures were performed at Bakircay University. For each TL measurement, approximately 23 mg of $GdBa_3B_9O_{18}$ powder was gently homogenized and subsequently compressed into circular pellets (6 mm in diameter) using a manual hydraulic press. This preparation method ensured consistent geometry and

improved thermal coupling during the heating process. To ensure reproducibility and minimize variability arising from sample inhomogeneity, all prepared pellets were subjected to a preliminary screening process prior to TL measurements. Each pellet was irradiated under identical conditions and its TL response was recorded. Only those samples exhibiting consistent glow-curve shape and integrated TL intensity within ±5% deviation were selected for further analysis. This procedure ensured that the reported TL characteristics are representative of homogeneous and reproducible sample behavior.

After irradiation, TL glow curves were recorded by heating the samples from room temperature to 450 °C under a controlled linear heating program. A heating rate of 2 °C s^{-1} was initially selected to obtain reference glow curves. Throughout the readout process, a constant nitrogen atmosphere was maintained to prevent oxidation and to eliminate possible chemiluminescence contributions.

3. Results and discussions

3.1. Crystal structure and phase analysis of $GdBa_3B_9O_{18}$

The X-ray diffraction (XRD) pattern confirms the formation of single-phase $GdBa_3B_9O_{18}$ (Fig. 1). All observed reflections were successfully indexed to the hexagonal space group $P6_3/m$ (No. 176), consistent with the crystallographic data reported for the $RBa_3B_9O_{18}$ (R = rare earth) structural family [37].

The refined lattice parameters were found to be $a = 7.1934(6)$ Å, $c = 17.206(3)$ Å, with $Z = 2$. These values are in excellent agreement with the data reported for $GdBa_3B_9O_{18}$ in the isostructural series described by Li et al. [37], confirming accurate formation of the target phase. No secondary phases were detected within the instrumental resolution. Structurally, the $RBa_3B_9O_{18}$ framework consists of planar B_3O_6 groups arranged in parallel layers along the *c*-axis, interconnected through regular REO_6 octahedra and BaO_6/BaO_9 polyhedral [37]. Within this structure, Gd^{3+} ions occupy octahedrally coordination sites, suggesting that isovalent RE^{3+} dopants preferentially substitute at the Gd site without charge compensation. This structural feature is relevant for the interpretation of the luminescence and TL behaviour.

3.2. Thermoluminescence emission selectivity and trap hierarchy analysis

3.2.1. Optical filter validation and recombination channel isolation

The TL emission of $GdBa_3B_9O_{18}$ was first evaluated using three optical filter combinations (BSL-TL-365 nm, IRSL-TL 410 nm, and IRSL-TL 565 nm) [38] in order to identify the dominant radiative recombination channel prior to kinetic analysis. Thermoluminescence emission was recorded using the standard filter sets of the Lexsyg Smart system. The UV-selective configuration (BSL–TL 365 nm) employs a U-340 glass filter combined with a BP365/50 interference filter, transmitting predominantly in the ~340–390 nm range while efficiently suppressing visible and infrared components. The blue-selective configuration (IRSL–TL 410 nm) uses a BG-39 glass filter together with an HC414/46 interference filter, providing a spectral window centered around ~410–415 nm with an effective passband of approximately 390–440 nm. The green-selective configuration (IRSL–TL 565 nm) consists of BG-39 combined with an HC575/25 interference filter, yielding transmission in the ~565–580 nm region with strong attenuation of UV/blue and red/IR contributions. A broadband blue detection mode (BG39 + BG25 + KG3) is also available for wideband TL/IRSL signals but was not used in the present kinetic analysis. Similar filter combinations and their dosimetric applications have been reported for $Ca_3Al_2O_6$ phosphors, where they were used to discriminate UV, blue, and green emission bands [38]. As shown in Fig. 2**a**, the IRSL-TL 410 nm configuration yielded the highest and most reproducible signal intensity over the entire glow curve, with clearly resolved maxima centered near 124 °C and 354 °C.

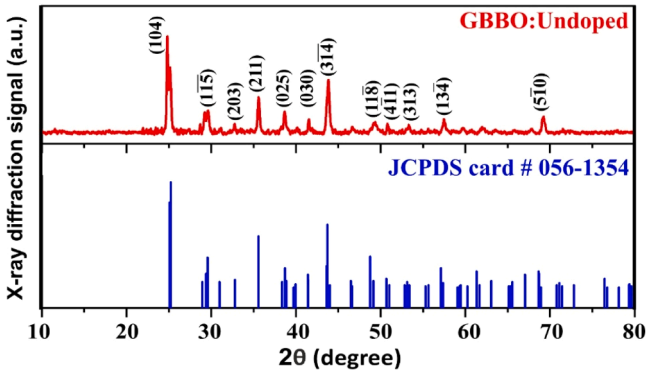

Fig. 1. Powder X-ray diffraction (XRD) pattern of $GdBa_3B_9O_{18}$ recorded at room temperature. All reflections can be indexed to the hexagonal space group $P6_3/m$ (No. 176).

In contrast, the 365 nm channel produced a significantly weaker response, while the 565 nm emission band remained comparatively minor and poorly structured. The systematic enhancement observed at 410 nm suggests that this spectral region corresponds to the primary recombination pathway in the present host lattice. Spectral selectivity in TL/IRSL measurements has been shown in several oxide and borate systems to influence the apparent trap contribution by preferentially probing specific recombination channels, thereby modifying peak ratios and kinetic interpretations [15,28,39]. Rather than merely selecting the highest-intensity channel, this step effectively isolates the dominant radiative center, minimizing spectral convolution from secondary or competing recombination processes.

Such emission selectivity is particularly important in borate-based systems, where multiple intrinsic and defect-related luminescence centers may coexist. By restricting subsequent analysis to the 410 nm channel, the trap characterization is performed under spectrally controlled conditions, thereby improving the physical reliability of the extracted kinetic trends. All further TL and preheat analyses were therefore conducted using the IRSL-TL 410 nm configuration.

3.2.2. Preheat-induced redistribution of trap population and initial rise evaluation

To probe the stability and energetic distribution of trapping centers, systematic preheating experiments were performed between 50 and 200 °C prior to TL readout (Fig. 2**b**). As clearly observed in Fig. 2**b**, increasing the preheat temperature progressively suppresses the low-temperature shoulder and reduces the relative intensity of the ~124 °C peak, while the higher-temperature region (~354 °C) remains comparatively more stable.

This behavior indicates thermally assisted emptying of shallow traps during the preheating stage, resulting in a redistribution of the trapped-carrier population before measurement. The inset of Fig. 2**b** shows the activation energy (E_a) values derived from the initial rise (IR) method as a function of preheat temperature, exhibiting a monotonic increasing trend rather than a constant plateau.

In discrete trap systems, a well-defined plateau in E_a versus T_{stop} is typically expected when a single isolated trap is thermally selected. However, no plateau region is evident in the E_a–T_{stop} relationship presented in Fig. 2**b**, suggesting either (i) closely spaced overlapping glow peaks or (ii) an energetically distributed trap population. Comparable E_a–T_{stop} behaviours have been reported in complex oxide and borate hosts, where continuous or mixed discrete–distributed trap architectures were inferred from combined IR/T_{stop} and glow-curve deconvolution analyses [3,28]. In particular, gradual E_a evolution with T_{stop} has been interpreted as characteristic of energetically distributed or strongly overlapping trap systems [40]. Given the continuous evolution of E_a without abrupt transitions, the present results are consistent with a non-isolated trap structure. Further discrimination between overlapping

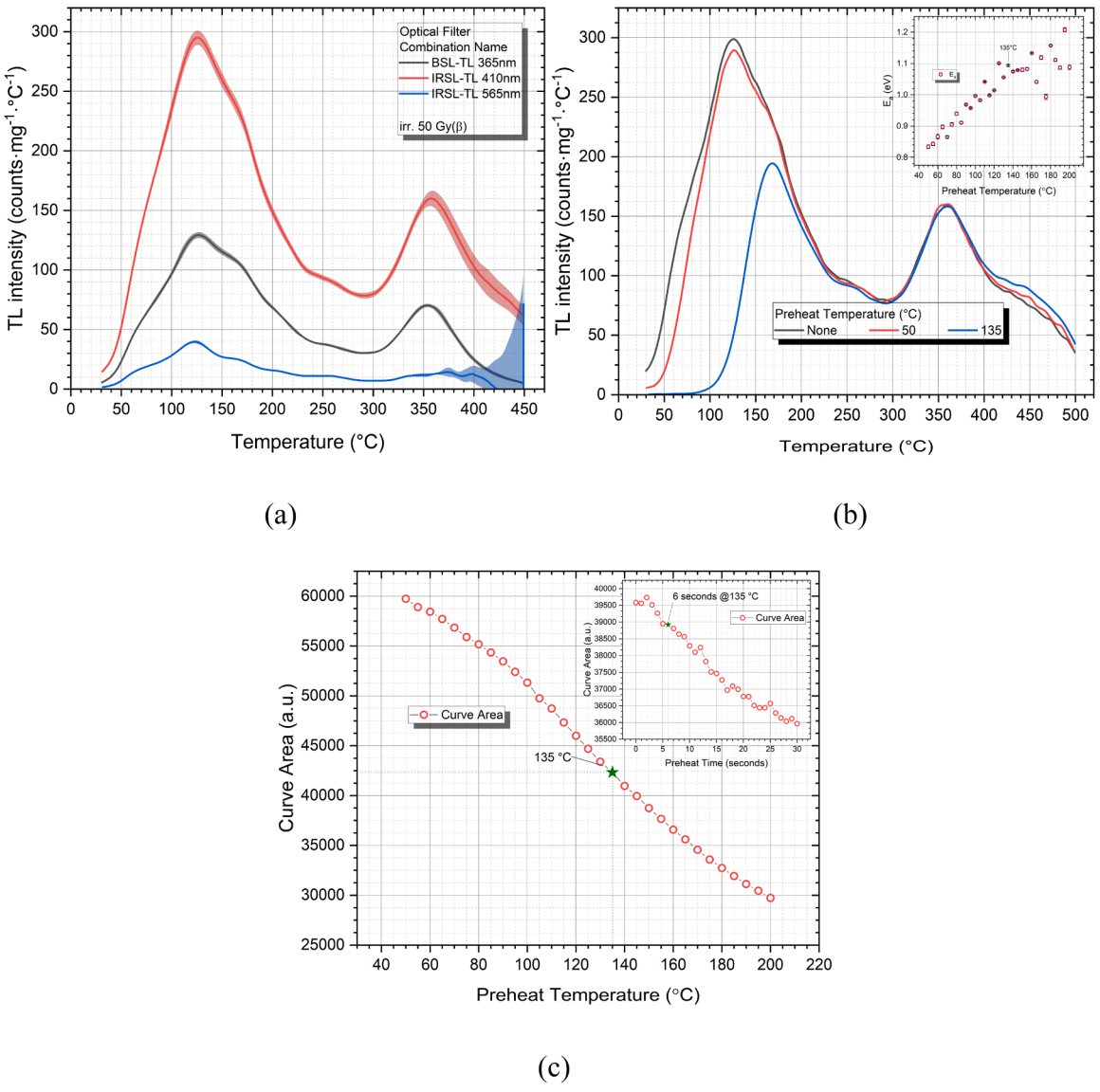

Fig. 2. (a) TL glow curves of $GdBa_3B_9O_{18}$ (50 Gy, β-irradiation) recorded using 365, 410, and 565 nm optical filters. The 410 nm configuration yields the dominant emission signal. Shaded regions indicate standard deviation (n = 3). (b) Effect of preheat temperature (50–200 °C) on the TL glow curve measured at 410 nm. Increasing preheat suppresses the low-temperature region. Inset: activation energy (E_a) derived from the initial rise method versus preheat temperature. (c) Integrated TL curve area as a function of preheat temperature. The monotonic decrease without a plateau suggests distributed trap depopulation. Inset: curve area variation with preheat time at 135 °C.

discrete traps and a distributed spectrum requires complementary kinetic analysis, which is presented in the subsequent sections using variable heating rate (VHR) and computerized glow-curve deconvolution **(**CGCD) approaches. These findings suggest that the trap population may be better described by a hierarchical structure with energetically distributed components rather than a simple two-level discrete model, contributing collectively to the composite glow curve.

3.2.3. Preheat-Induced Trap Evolution and Structural Implications

Further insight into the trap architecture is obtained from the evolution of the total glow curve area as a function of preheat temperature (Fig. 2**c**). The integrated TL signal decreases monotonically with increasing preheat temperature, and no plateau region is observed throughout the investigated range.

In discrete trap models, a plateau in the glow curve area typically indicates that all shallow traps have been removed while deeper traps remain unaffected. The continuous reduction observed here suggests progressive depopulation across a spectrum of trap depths rather than stepwise elimination of isolated levels. The absence of stabilization even near 135 °C supports the interpretation of an energetically distributed or overlapping trap structure.

Similar monotonic area reduction trends have been discussed in the context of distributed trap density profiles, where integrated TL intensity is used as an indirect probe of trap population evolution across an energy continuum [40]. The inset of Fig. 2**c** further illustrates the evolution of the integrated TL area as a function of preheating time at 135 °C. The progressive reduction of signal with increasing holding time indicates that trap depopulation is not governed solely by temperature threshold effects but also by thermally activated time-dependent release processes. The absence of a saturation plateau within the investigated time window suggests that traps contributing to the composite glow curve possess a range of thermal lifetimes rather than a single well-defined decay constant. Such behavior is consistent with a hierarchical or energetically distributed trap system, where progressively deeper or less probable escape pathways remain active during extended preheating.

From a structural standpoint, this behavior may plausibly be associated with the Ba-rich trigonal lattice of $GdBa_3B_9O_{18}$. Compared with Al-centered borate frameworks such as $GdAl_3(BO_3)_4$ or $Li_3Al_3(BO_3)_4$:Gd, the present topology provides a distinct cation coordination environment and charge-compensation landscape. Variations in local coordination symmetry and defect-complex formation have previously been correlated with modifications in trap depth distributions in rare-earth borates and related oxide hosts [41,42]. Such structural differences can plausibly modify defect complex formation, alter retrapping probability, and broaden the energetic distribution of trapping states. While this interpretation remains mechanistic and requires confirmation through glow-curve deconvolution or complementary kinetic techniques, the present preheat and area analyses consistently indicate a non-discrete trap hierarchy.

The absence of a plateau in the E_a–T_{stop} relationship, together with the monotonic decrease of the integrated glow-curve area under progressive preheating, indicates that the trap system in $GdBa_3B_9O_{18}$ cannot be described by a simple two-level discrete model. These observations are consistent with either closely overlapping discrete traps or an energetically distributed trap hierarchy.

Considering the Ba-rich trigonal topology of $GdBa_3B_9O_{18}$ and its coordination environment distinct from Al-centered borate systems, a broadened defect landscape may be expected. Such structural characteristics can lead to a wider distribution of local trapping configurations and, consequently, to a distributed trap-depth spectrum. To evaluate this structural interpretation, complementary kinetic analyses are applied in the following sections. Variable Heating Rate (VHR), T_m–T_{stop} /Initial Rise (IR) comparison, and Computerized Glow Curve Deconvolution (CGCD) are used to determine whether the extracted kinetic parameters converge toward discrete trap behavior or support an energetically distributed trap model.

3.3. Dose response characteristics and minimum detectable dose

The dose–response behavior of $GdBa_3B_9O_{18}$ was investigated using the integrated glow-curve area recorded at 410 nm, corresponding to

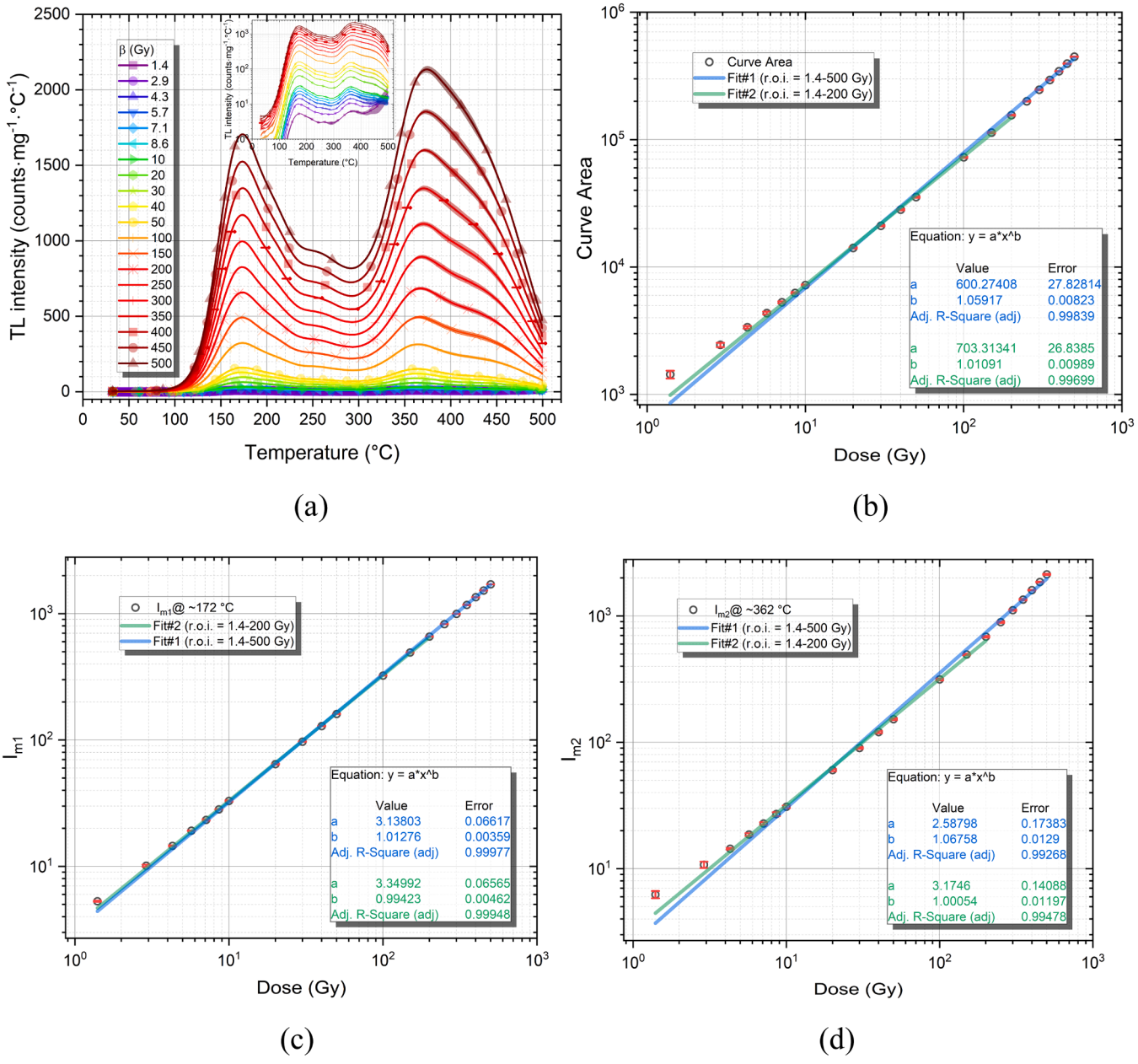

Fig. 3. Dose–response characteristics of $GdBa_3B_9O_{18}$ recorded at 410 nm under β-irradiation.

the spectrally isolated dominant recombination channel identified in Section 3.2. All TL measurements were performed under identical readout conditions following β-irradiation in the range 1.4–500 Gy.

As shown in Fig. 3**a**, the glow curves exhibit a systematic increase in intensity with increasing dose while maintaining their overall structural profile. The two dominant components centered near ~172 °C and ~362 °C remain clearly resolved across the entire dose range. No significant peak shift or saturation behavior is observed up to 500 Gy, indicating stable recombination dynamics within the investigated interval. The preservation of the glow-curve topology across dose suggests that the relative trap architecture remains stable within the investigated excitation regime.

The quantitative dose–response of the integrated TL area is presented in Fig. 3b. The data were fitted using a power-law function of the form $y = a \bullet x^b$. Two fitting intervals were considered to evaluate linearity. Within the 1.4–200 Gy range, the fitted exponent is $b = 1.0109 \pm 0.0099$ (Adj. $R^2 \approx 0.997$), demonstrating near-ideal linear behavior within experimental uncertainty. This region is therefore defined as the primary linear calibration range for dosimetric applications [43].

When the fitting interval is extended to 500 Gy, the exponent increases to $b = 1.0597 \pm 0.0082$ (Adj. $R^2 \approx 0.998$), indicating mild supralinearity at higher doses. Such behaviour is commonly reported in TL materials and is generally attributed to dose-dependent variations in trap filling, retrapping probability, or competition among recombination pathways [44–46]. In the present case, the slightly stronger deviation observed for the high-temperature component (I_{m2}) may reflect an increased contribution from thermally more stable or kinetically less accessible trapping states as the excitation density increases. Notably, the preservation of the overall glow-curve topology across the investigated dose range suggests that this supralinear trend is governed primarily by population dynamics rather than structural modification of trapping centers.At this stage, this interpretation remains phenomenological, and detailed kinetic clarification will be provided through VHR and CGCD analyses in subsequent sections.

To verify the robustness of the area-based dosimetric approach, the dose dependence of the individual glow components was analysed separately. The ~172 °C peak (I_{m1}), shown in Fig. 3c, exhibits near-unity dose exponents up to 200 Gy and only minor deviation from linearity in the extended range. Similarly, the high-temperature peak (~362 °C, I_{m2}), presented in Fig. 3d, follows linear scaling within the primary interval and displays a slightly more pronounced supralinear tendency at higher doses. The consistent behaviour of both components supports the reliability of the integrated glow-curve area as a stable dosimetric metric.

The minimum detectable dose (MDD) was determined using the 3σ criterion according to [47]:

$$D_{LDL} = 3\sigma_{Bkg}\Phi_c$$

where σ_{Bkg} represents the standard deviation of the mean background signal and Φ_c is the calibration factor defined as the ratio between delivered dose (Gy) and the corresponding net integrated TL area obtained within the primary linear range (1.4–200 Gy). Using this approach, the calculated value is: MDD = 106.95 ± 19.45 mGy; indicating sub-Gy detection capability under the present experimental conditions. Background values were determined from repeated non-irradiated measurements under identical readout conditions. Considering the established linear response between 1.4 and 200 Gy and the absence of saturation up to 500 Gy, the obtained MDD positions $GdBa_3B_9O_{18}$ primarily within medium-to-high-dose dosimetry applications. While the sensitivity does not reach the sub-mGy levels reported for highly optimized low-dose medical or environmental dosimeters [48,49], comparable MDD values in the ~0.1 Gy regime have been reported for TL materials developed primarily for medium-to-high-dose applications, where dynamic range and linearity are prioritized [50,51]. In this context, the present material demonstrates stable response characteristics across an extended high-dose interval. Accordingly, its performance is better suited for applications where dose dynamic range and linearity in the Gy regime are more critical than ultra-low detection thresholds.

Overall, the combined analysis of Fig. 3**a–d** demonstrates a well-defined primary linear response region (1.4–200 Gy), followed by a moderately supralinear extension up to 500 Gy, without evidence of saturation or structural instability in the glow curve. These characteristics confirm the suitability of $GdBa_3B_9O_{18}$ for medium-to-high-dose dosimetric applications and provide a consistent framework for subsequent kinetic validation of the underlying trap architecture.

To contextualize the dosimetric performance of $GdBa_3B_9O_{18}$ within the broader family of borate-based TL materials, a comparison with representative borate hosts is summarized in Table 1.

As shown in Table 1, lithium borates are optimized for ultra-low dose sensitivity, whereas Ba-containing borates, including $GdBa_3B_9O_{18}$, operate predominantly in medium-to-high-dose regimes characterized by extended linearity and stable reusability. Thus, the present material is positioned toward applications where wide dynamic range and structural stability are prioritized over sub-mGy detection thresholds.

(a) TL glow curves for doses between 1.4 and 500 Gy. (b) Integrated glow-curve area as a function of dose with power-law fits for 1.4–200 Gy and 1.4–500 Gy ranges. (c) Dose response of the ~172 °C peak (I_{m1}). (d) Dose response of the ~362 °C peak (I_{m2})

3.4. Reusability and signal stability

The reusability of $GdBa_3B_9O_{18}$ was evaluated through ten consecutive irradiation–readout cycles at a fixed dose of 50 Gy under identical experimental conditions. The mean TL glow curves for each readout are presented in Fig. 4**a**, while the corresponding normalized integrated glow-curve area values are shown in Fig. 4**b**.

As observed in Fig. 4a, the overall glow-curve topology remains preserved throughout the repeated cycles. The two dominant components centered near ~172 °C and ~362 °C retain their relative intensities and peak positions without measurable shift or distortion. No systematic broadening or progressive suppression of the high-temperature tail is observed. The preservation of the glow-curve structure indicates that the trapping–recombination framework remains stable under repeated irradiation and readout operations.

A quantitative evaluation was performed by normalizing the integrated TL area of each cycle to the first readout (Fig. 4**b**). The maximum deviation from the initial value remains well within the ±5% deviation band, with an average deviation of approximately −0.4% from the mean and −0.5% relative to the first cycle. Importantly, no monotonic drift or cumulative signal degradation is observed across successive measurements.

The absence of progressive signal loss suggests that the irradiation–readout sequence does not induce cumulative modification of the active trapping or recombination centers within experimental resolution. In particular, the stability of the high-temperature component implies that thermally stable trapping states are not permanently depleted or structurally altered during the applied cycles. Such behavior is consistent with a robust trapping architecture capable of sustaining repeated excitation without measurable structural modification.

Reproducibility levels within a ± 5% deviation band are widely regarded as acceptable for practical Gy-range dosimetry in contemporary irradiation and detector performance studies [52,53]. The cycle-to-cycle variation observed here therefore lies comfortably within commonly reported tolerance levels.

From a dosimetric perspective, the low cycle-to-cycle variation and structural reproducibility confirm that $GdBa_3B_9O_{18}$ exhibits reliable reusability under medium-dose conditions. The material therefore satisfies an essential requirement for practical TL dosimetry, where signal repeatability and structural stability are critical for calibration integrity.

Table 1
Representative borate-based TL materials illustrating typical minimum detectable dose (MDD) levels and operating dose regimes. Values compiled from literature to indicate general application domains rather than strict performance ranking.

Material (Host: Dopant)	Approx. MDD (Gy)	Primary Linear Dose Range (Gy)	Stability / Reusability (Qualitative)	Typical Application Focus	Reference
$Li_2B_4O_7$:Cu,Ag	~10^{-3} –10^{-2}	~10^{-3} –10 [1] (dose-dependent)	Good reproducibility; well-resolved glow-curve structure	Low-dose medical / environmental dosimetry	[22,28]
$Li_2B_4O_7$:Cu	~10^{-3} –10^{-2}	Up to a few Gy	Improved cycle stability and signal repeatability	Low-dose X-ray / γ dosimetry	[23]
MgB_4O_7:Dy^{3+}	~10^{-2}–10^{-1}	Low-dose β region	Stable TL response in low-dose regime	Low-dose β dosimetry	[20]
$NaBaBO_3$:Gd^{3+}	~10^{-2}–10^{-1}	Up to tens of Gy	Detailed trap analysis; moderate reusability	Medium-dose β dosimetry	[33]
$GdBa_3B_9O_{18}$	0.107 ± 0.019	1.4–200 (linear); 1.4–500 (mild supralinear)	Reusability within ±5% over ≥ 10 cycles; stable glow-curve profile	Medium-to-high dose Gy-range dosimetry	This work

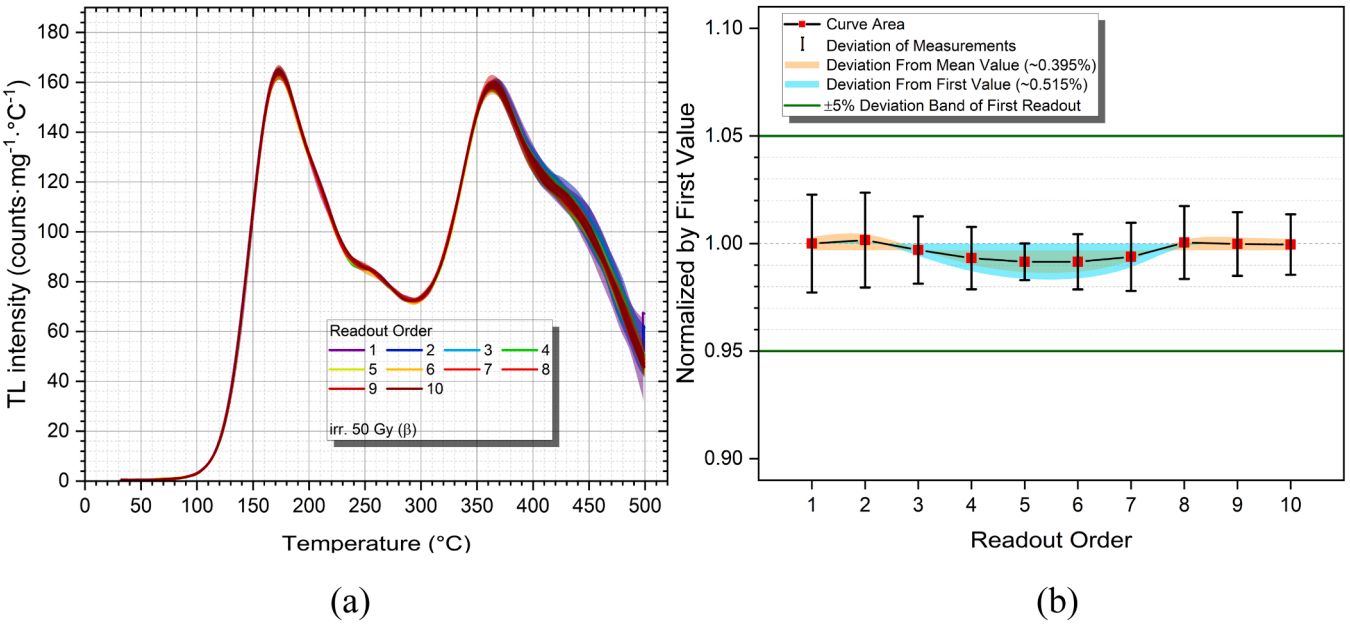

Fig. 4. (a) Reusability test of the TL glow curves recorded after repeated 50 Gy β-irradiation (1–10 readouts), showing consistent peak shape and intensity. (b) Normalized integrated TL area as a function of readout order; the deviation from the first measurement remains within ±5%, indicating stable signal reproducibility.

3.5. Heating rate dependence and temperature lag correction

The influence of heating rate on the TL response of $GdBa_3B_9O_{18}$ was investigated by recording glow curves at β = 0.5–4 °C s^{-1} after β-irradiation of 50 Gy (Fig. 5**a**). As the heating rate increases, both glow peaks shift systematically toward higher temperatures. This is generally expected from standard TL kinetic theory, where the glow-peak maximum occurs at higher temperatures when the system is heated more rapidly under linear heating conditions [54,55].

To quantify the heating-rate dependence, the integrated TL area together with the peak temperatures (T_{m1}, T_{m2}) and peak intensities (I_{m1}, I_{m2}) were normalized to the values obtained at the lowest heating rate and plotted as a function of β (Fig. 5**b**). The results show a monotonic increase of T_m with increasing β, accompanied by a slight reduction in peak intensity and integrated TL area at higher heating rates. Similar trends have been reported in various oxide and borate TL materials and may plausibly arise from non-equilibrium recombination conditions and possible thermal quenching effects at elevated heating rates [15,56,57], although a quantitative separation of these mechanisms would require detailed kinetic modelling.

Because apparent peak shifts may also arise from thermal lag between the heater and the sample, a temperature-lag correction was applied using the method proposed by Kitis and Tuyn [58]. The corrected and uncorrected peak temperatures for the two main glow peaks are compared in Figs. 5**c** and 5**d**. The correction produces a small but systematic reduction in T_m at higher heating rates, while preserving the overall $T_m(\beta)$ dependence.

The magnitude of the applied temperature-lag correction for both glow peaks remains relatively small across the investigated heating-rate range, as summarized in Table 2, where the maximum correction does not exceed approximately 3–4 °C even at β = 4 °C s^{-1} .

This suggests that the dominant contribution to the observed peak displacement is likely related to intrinsic TL kinetics rather than instrumental temperature lag. Overall, the heating-rate analysis confirms the expected kinetic behaviour of the glow peaks and demonstrates that temperature-lag effects are minor under the present experimental conditions.

4. Kinetic characterization

4.1. Various heating-rate (VHR) methods for activation energy determination

To determine the trap depth associated with the dominant TL glow peaks, the activation energy was evaluated using several VHR–based approaches. These methods exploit the systematic shift of the glow-peak maximum temperature (T_m) with the linear heating rate (β) and allow the trap parameters to be extracted without requiring a full kinetic deconvolution of the glow curve.

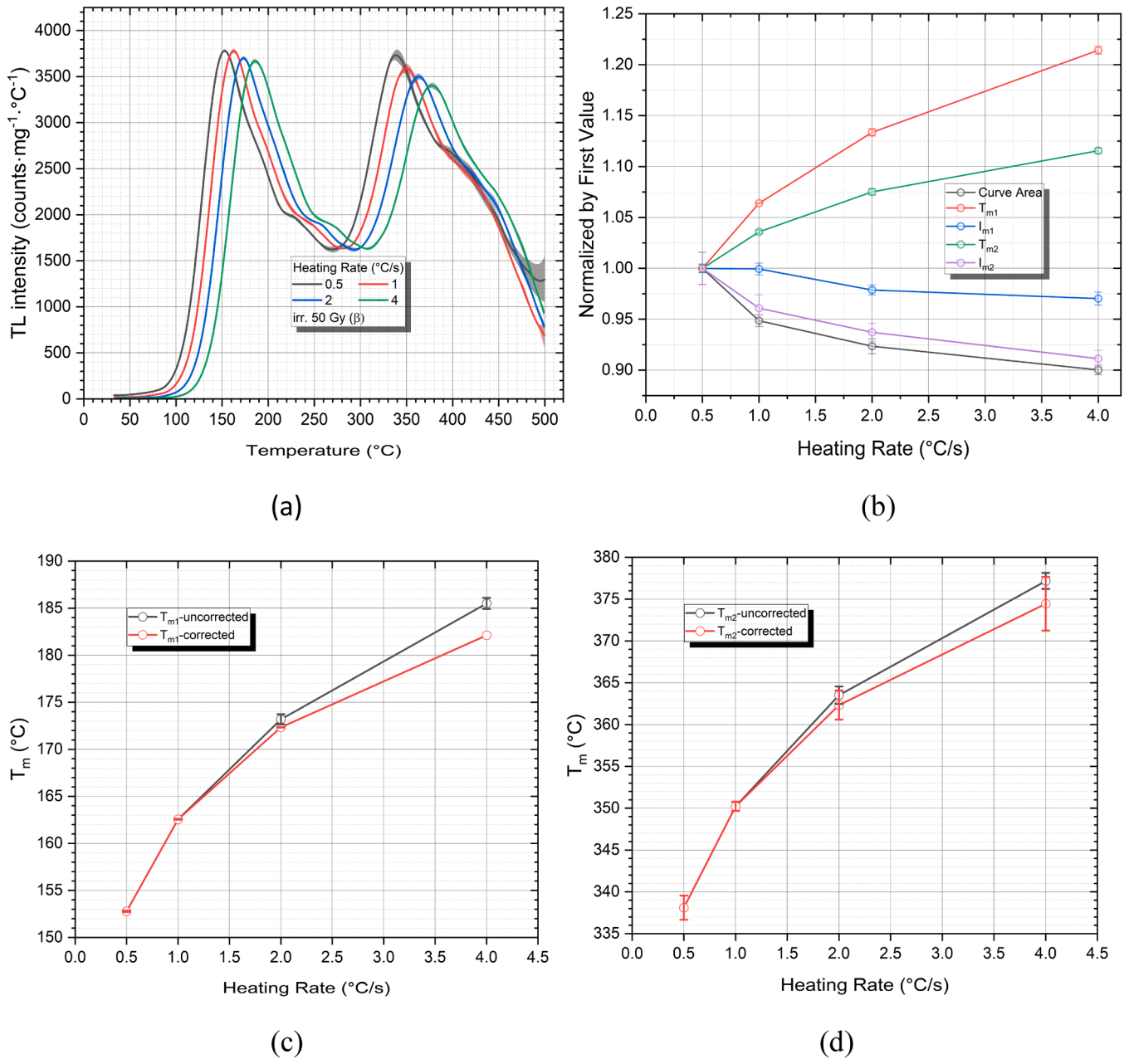

Fig. 5. Heating-rate dependence of the TL response of $GdBa_3B_9O_{18}$ (50 Gy). (a) Glow curves recorded at 0.5–4 °C s^{-1} . (b) Normalized TL parameters (area, T_{m1}, T_{m2}, I_{m1}, I_{m2}) versus heating rate. (c) Uncorrected and temperature-lag-corrected peak temperature for the first glow peak (T_{m1}). (d) Corresponding comparison for the second glow peak (T_{m2}) using the Kitis–Tuyn temperature-lag correction.

Table 2
Summary of the temperature-lag corrections for the two TL glow-peak maxima.

Heating Rate (°C/s)	ΔT_{m1} (°C)	ΔT_{m2} (°C)
0.5	0 ± 0	0 ± 0
1	0 ± 0	0 ± 0
2	0.85 ± 0.56	1.18 ± 0.99
4	3.39 ± 0.59	2.72 ± 4.13

(i) Hoogenstraaten method [59]

In the classical VHR formulation proposed by Hoogenstraaten [59], the shift of the glow-peak maximum temperature with heating rate is analyzed through the linear relation between $\ln(T_m^2/\beta)$ and $1/T_m$. The slope of this plot yields the activation energy (E), while the intercept yields the frequency factor (s). Although originally derived for first-order kinetics, later studies have shown that the method can provide reliable estimates of activation energies not only for first-order but also for general-order TL peaks and more complex recombination schemes [60,61].

(ii) Booth–Bohun–Parfianovitch (two-rate) method [62–64]

The Booth–Bohun–Parfianovitch method [62–64] represents a simplified two-rate implementation of the VHR approach. In this formulation [65],

$$E_a = k\frac{T_{m_1}T_{m_2}}{T_{m_1}-T_{m_2}}\ln\left[\frac{\beta_1}{\beta_2}\left(\frac{T_{m_2}}{T_{m_1}}\right)^2\right]$$

the activation energy is determined from the temperatures of the same TL peak measured at only two different heating rates. By

relating the difference in T_m values corresponding to the two heating rates to the activation energy through a closed-form expression, the method enables rapid estimation of the trap depth and effective frequency factor. Previous studies have shown that this approach can provide reasonable kinetic estimates for general-order glow peaks when appropriate heating-rate pairs are selected [15,66].

(iii) Gartia et al. [67] evaluation of VHR methods

Gartia et al. [67] performed a critical assessment of several VHR-based procedures by combining numerical simulations with experimental TL data. Their analysis examined the influence of kinetic order and peak parameters on the accuracy of the extracted activation energies and demonstrated that commonly used VHR variants, including Hoogenstraaten-type formulations, can provide reliable activation energy estimates that are largely independent of the assumed kinetic model under realistic TL conditions [67].

Within this framework, the activation energy can be can be expressed according to Gartia et al. [67] as

$$E = k\frac{T_{m_1}T_{m_2}}{T_{m_1} - T_{m_2}}\ln\left[\left(\frac{I_{m_1}}{I_{m_2}}\right)\right]$$

where T_{m1} and T_{m2} are the peak temperatures obtained at two different heating rates, I_{m1} and I_{m2} represent the corresponding peak intensities, and k is the Boltzmann constant.

For this reason, several VHR formulations were applied in the present work to cross-validate the activation energies obtained from the heating-rate analysis.

4.1.1. Activation energy determination from VHR analysis

Fig. 6**a** and Fig. 6**b** present the Hoogenstraaten plots obtained for the first and second glow peaks, respectively. In these plots, $\ln(T_m^2/\beta)$ is represented as a function of $1/kT_m$ for both the uncorrected and temperature-lag-corrected peak temperatures.

As expected from the Hoogenstraaten formalism, the data exhibit a clear linear dependence over the investigated heating-rate range, indicating that the peak displacement with heating rate follows the thermally activated release kinetics assumed in the VHR model. The high linear correlation coefficients ($R^2 \approx 0.999$) obtained for both corrected and uncorrected datasets further confirm the internal consistency of the method and the reliability of the extracted kinetic parameters.

For the first glow peak, the slope of the Hoogenstraaten plot yields activation energies of approximately 1.00 ± 0.06 eV for the uncorrected temperatures and 1.11 ± 0.03 eV after applying the temperature-lag correction. A similar trend is observed for the second glow peak, where the activation energy increases from 1.72 ± 0.15 eV (uncorrected) to 1.86 ± 0.20 eV (corrected) as shown in Table 3. The slightly higher values obtained after lag correction are consistent with the reduction of the apparent peak temperature caused by thermal delay between the heater and the sample during high-rate measurements.

To further verify the robustness of the VHR analysis, activation energies were also calculated using the Booth–Bohun–Parfianovitch [62–64] two-rate method and the VHR evaluation framework discussed by Gartia et al. [67]. In these calculations, T_m values from each heating rate were paired with those obtained at the other rates, and the resulting activation energies were averaged for the corresponding methods. The resulting values are summarized in Table 3.

Overall, all three VHR approaches yield mutually consistent activation energies. The average effective activation energies obtained from the different methods fall in the ranges of ~1.05–1.17 eV for the first glow peak and ~1.70–1.89 eV for the second glow peak, depending on whether temperature-lag correction is applied (see Table 3). The agreement among the independent VHR procedures indicates that the obtained trap depths are robust with respect to the specific analysis method and kinetic assumptions.

The slightly larger activation energies obtained after temperature-lag correction further support the conclusion that thermal lag introduces a small systematic bias in peak-temperature determination at higher heating rates. However, the relatively modest magnitude of this correction confirms that the intrinsic TL kinetics dominate the observed heating-rate dependence of the glow peaks under the present experimental conditions.

It should be emphasized that the activation energies obtained from the VHR methods for the two dominant TL maxima represent effective trap depths associated with composite glow-peak envelopes, rather than single, isolated trapping levels. IR–T_m–T_{stop} diagnostics and CGCD analysis clearly reveal a hierarchical and energetically distributed trap

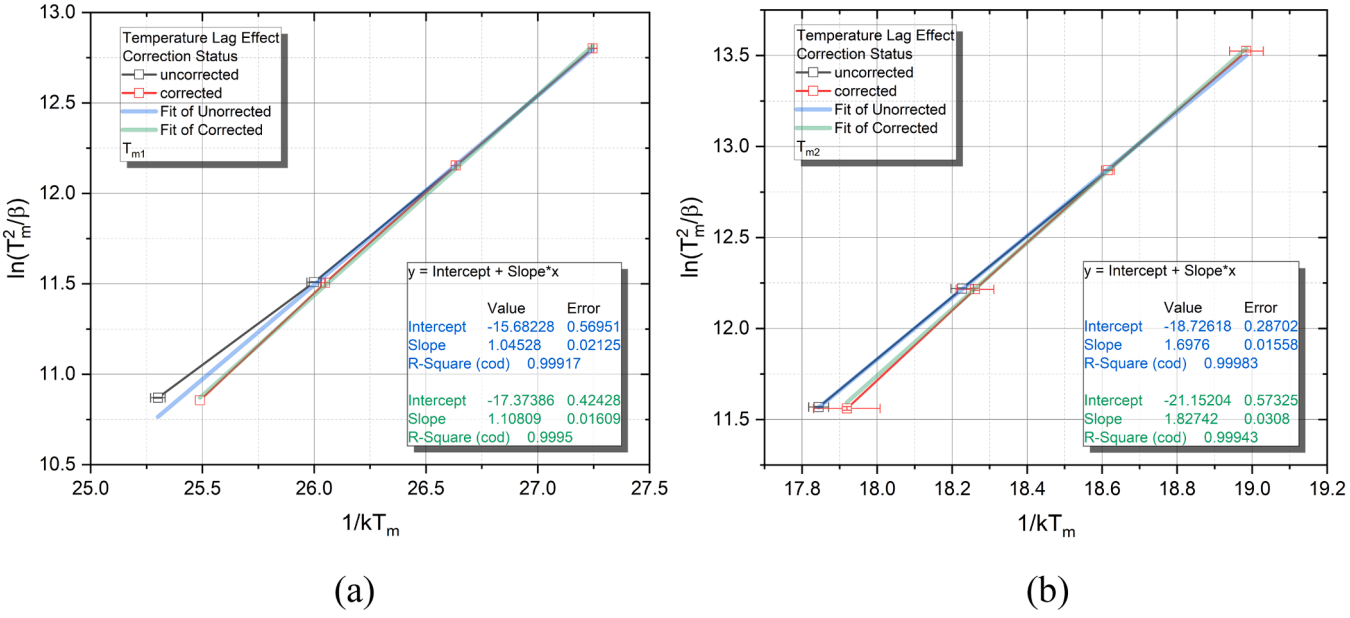

Fig. 6. Hoogenstraaten plots used for activation energy determination of the two dominant TL glow peaks of $GdBa_3B_9O_{18}$. The linear dependence of $\ln(T_m^2/\beta)$ on $1/T_m$ is shown for both uncorrected and temperature-lag corrected peak temperatures: (a) first glow peak (T_{m1}) and (b) second glow peak (T_{m2}). Solid lines represent the linear fits used to extract the activation energy from the slope.

Table 3
Effective activation energies of the two main composite TL maxima obtained from VHR methods.

Calculated Effective E_a (eV)					
β (°C/s)	***Temp. Lag Effect Status***				***Method***
	Maximum 1		***Maximum 2***		
	Uncorrected	***Corrected***	***Uncorrected***	***Corrected***	
Average of Pairs of 0.1–4	1.00 ± 0.06	1.11 ± 0.03	1.72 ± 0.15	1.86 ± 0.20	Booth-Bohun-Parfianovitch Method [62–64]
0.1–10	1.05 ± 0.02	1.11 ± 0.02	1.70 ± 0.02	1.83 ± 0.03	Hoogenstraaten's Method [59]
Average of Pairs of 0.1–10	1.06 ± 0.06	1.17 ± 0.03	1.75 ± 0.14	1.89 ± 0.19	Gartia et al. [67]

spectrum ($E_a \approx 0.87$–1.98 eV), with multiple overlapping components contributing to each main maximum. In this context, the VHR-derived activation energies should be interpreted as average energy barriers governing thermal release from the dominant subset of traps responsible for the low- and high-temperature maxima under the applied heating-rate conditions.

The frequency factors obtained for the ~168 °C and ~352 °C components are on the order of 10^{12}–10^{13} s^{-1}, which lies within the typical range reported for TL borate phosphors. However, in a general-order system with overlapping trap distributions, these values should not be interpreted using the simple first-order lifetime expression ($\tau \approx s^{-1}\exp(E/kT)$) valid for isolated traps. Instead, the effective storage time at ambient conditions is governed by the full kinetic framework (E, s, b), as well as retrapping and charge redistribution processes, as evidenced by the IR–T_m–T_{stop} and CGCD analyses. Furthermore, within a hierarchical and energetically distributed trap spectrum ($E_a \approx 0.87$–1.98 eV), carriers thermally released from shallower traps can be retrapped into deeper, more stable states. This dynamic significantly extends the effective macroscopic lifetime, meaning that simple single-trap estimates can substantially underestimate the observed signal stability. The experimentally observed TL stability (including anti-fading behavior over ~12 h) is therefore fully consistent with the extracted trap hierarchy. This interpretation is further supported by the CGCD analysis presented in the following section, which resolves the composite glow peaks into multiple overlapping components.

4.2. Kinetic diagnostics based on IR and T_m–T_{stop} analysis

The kinetic behavior of $GdBa_3B_9O_{18}$ was examined using a combined Initial Rise (IR) and T_m–T_{stop} approach, which enables diagnostic probing of trap structure without assuming a specific global kinetic model. Under linear heating conditions, the glow peak maximum temperature (T_m) corresponds to the temperature at which the thermally activated release probability of trapped carriers becomes comparable to the applied heating rate. T_m is therefore directly related to trap depth and escape probability [55,68].

In the T_m–T_{stop} protocol, the sample is irradiated, preheated to progressively higher stop temperatures (T_{stop}), rapidly cooled, and subsequently subjected to a full TL readout. Progressive preheating selectively removes carriers from shallower traps, allowing deeper trapping states to dominate the remaining glow curve. In ideal discrete first-order systems, this procedure yields plateau regions in the T_m–T_{stop} relationship, each corresponding to a thermally isolated trapping level. In contrast, systems with continuous or strongly overlapping traps typically show smoothly varying T_m–T_{stop} curves rather than well-defined plateaus [69,70].

The IR method was applied to the low-temperature flank of the selected glow peaks, where the TL intensity follows an exponential dependence,

$$I(T) \propto \exp(-E_a/kT)$$

In this regime, retrapping effects are minimized and the activation energy (E_a) can be locally estimated without strict assumptions regarding kinetic order [15]. However, in materials containing overlapping glow peaks or energetically distributed traps, the extracted E_a represents an effective (apparent) activation energy that evolves with the progressively selected trap population rather than a single invariant structural parameter.

The glow curves recorded after successive T_{stop} treatments are shown in Fig. 7**a**. With increasing preheat temperature, the low-temperature component is progressively suppressed, indicating selective depopulation of shallow traps. The evolution of the glow curve is gradual rather than stepwise, and no extended T_{stop} interval is observed in which a single invariant peak dominates the emission.

The IR-derived activation energies as a function of T_{stop} are presented in Fig. 7**b**. The E_a values increase monotonically from approximately 0.8 eV to nearly 2.0 eV, although the evolution occurs through several quasi-stable segments (P1–P12) highlighted in the figure rather than through a single continuous plateau. The inset T_m–T_{stop} relationship exhibits a similarly continuous shift toward higher temperatures. These locally grouped regions correspond to successive subsets of traps that dominate the TL emission after partial thermal cleaning. The activation energy values obtained from the IR analysis as a function of T_{stop} are summarized in Table 4. These IR-derived E_a intervals provide a quantitative basis for identifying physically meaningful trapping levels and for assessing whether apparent glow-curve features correspond to distinct traps or to overlapping components. The data are grouped into regions (A–G) corresponding to quasi-stable E_a intervals, which reflect dominant subsets of traps contributing to the TL emission. In Fig. 7(b), the labels P1–P12 do not represent individually fitted TL peaks based on only 1–3 experimental points. Rather, they denote quasi-stable E_a segments identified from the monotonic E_a–T_{stop} evolution obtained by the IR method over finite T_{stop} intervals, each comprising multiple measurements. The purpose of this segmentation is purely diagnostic: it highlights successive subsets of traps that dominate the TL emission after partial thermal cleaning and provides a qualitative estimate of the number of overlapping components contributing to the composite glow curve. In this framework, the identification of TL peaks is based on the stability of E_a values over finite T_{stop} intervals rather than on the number of experimental points defining local features in the glow curve. Regions exhibiting stable E_a values are interpreted as physically meaningful trapping levels or substructures.

Accordingly, the subsequent CGCD analysis (presented in the following section) does not fix the number of TL peaks a priori from Fig. 7(b). Instead, the number of components is determined through an iterative fitting procedure to achieve a physically meaningful representation of the composite glow curve, consistent with the continuously evolving E_a–T_{stop} behavior. These IR-derived regions are further

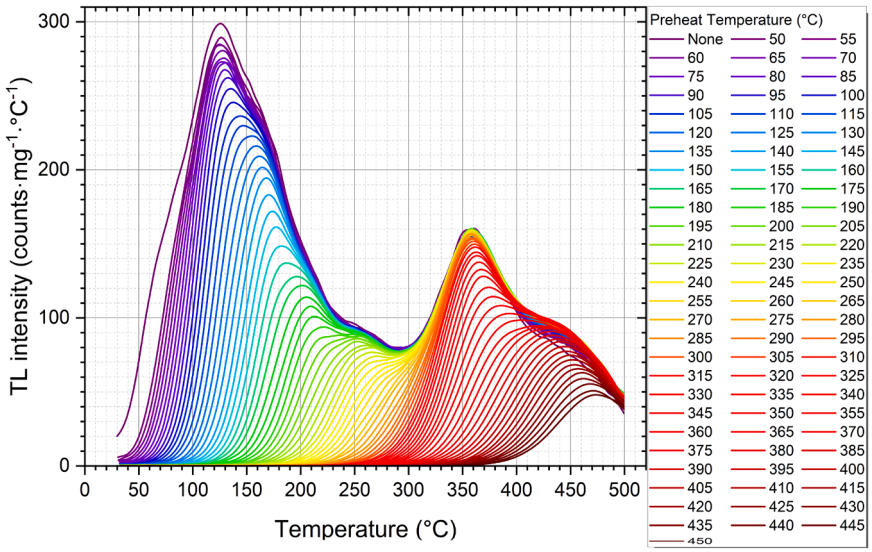

(a)

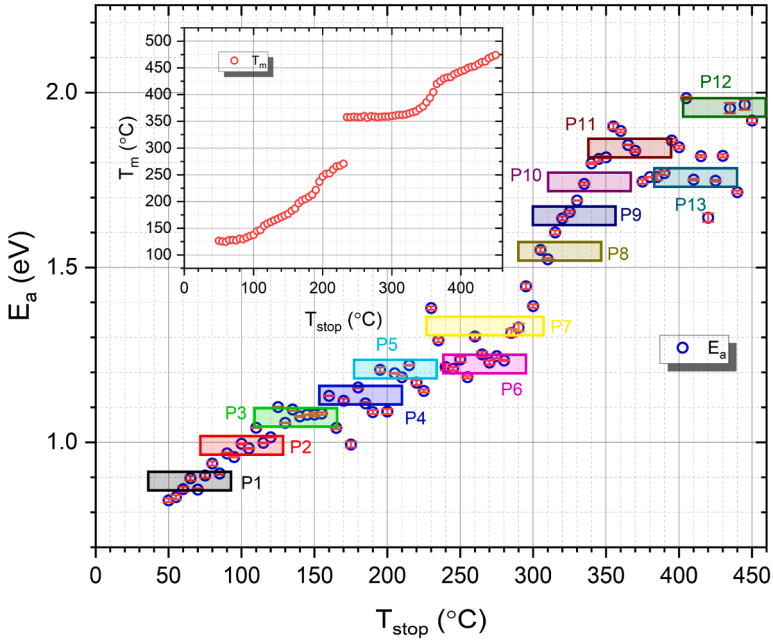

(b)

Fig. 7. Kinetic diagnostics of $GdBa_3B_9O_{18}$ based on the T_m–T_{stop} and Initial Rise (IR) analysis. (a) TL glow curves recorded after successive T_{stop} (partial cleaning) treatments (b) Activation energy E_a versus T_{stop} obtained by the IR method. The shaded P1–P12 intervals indicate quasi-stable E_a segments over finite T_{stop} ranges and are used only as qualitative guidance for the subsequent CGCD; they are not individual peaks fitted to single data points.

correlated with the CGCD peaks, providing a consistent framework linking the continuous E_a–T_{stop} evolution with the discrete representation obtained from glow curve deconvolution. Similar monotonic evolution of activation energy and plateau-free T_m–T_{stop} behavior have been reported for materials exhibiting overlapping glow peaks or energetically distributed trapping states, where the extracted E_a reflects the progressively evolving subset of occupied traps rather than a single invariant trap depth [28,40,55].

The activation energies obtained from the VHR analysis fall within the effective energy range estimated from the IR/T_{stop} diagnostics. Taken together, the combined IR and T_m–T_{stop} diagnostics indicate that the trapping structure of $GdBa_3B_9O_{18}$ cannot be adequately described by a single isolated discrete trap. The results are most conservatively interpreted as evidence that the dominant trap population evolves under partial cleaning, in a manner compatible with either closely spaced overlapping traps or a distributed trap hierarchy, without permitting a unique structural assignment based solely on IR/T_{stop} signatures.

4.3. Glow curve deconvolution (CGCD) analysis

To further resolve the trap structure contributing to the TL emission of $GdBa_3B_9O_{18}$, the experimental glow curve was analyzed using computerized glow curve deconvolution (CGCD). In this approach, the composite TL glow curve is represented as the superposition of several

Table 4
Activation energy (Ea) ranges obtained from the Initial Rise (IR) method as a function of Tstop, and their correspondence to CGCD components across different irradiation doses (50–150 Gy). The IR regions represent quasi-stable Ea intervals associated with dominant subsets of traps, while the CGCD peaks provide their discrete representation. The consistency across doses confirms the physical reliability of the identified trap structure.

IR Region	E_a Range (eV)	Mean E_a (eV)	CGCD Peaks (all doses)	Dose Stability	Interpretation
A	0.87–1.01	~0.94	1–2	Very stable	Single trap, subdivided in CGCD
B	1.09–1.13	~1.11	3–4	Very stable	Single trap
C	1.22	1.22	5–6	Identical across doses	Single trap, clearly split in CGCD
D	1.31	1.31	7	Stable	Single trap
E	1.55–1.64	~1.60	8–9	Very stable	Single trap, subdivided in CGCD
F	1.74–1.87	~1.80	10–11, 13	Stable	One or two traps, partially split
G	1.98	1.98	12	Very stable	Single deep trap

individual glow peaks, each described by a general-order kinetic expression. For a single glow peak, the TL intensity can be expressed as

$$I(T) = I_m \exp\left(\frac{E}{kT_m^2}(T - T_m)\right)\left[\frac{1}{b} + \frac{b-1}{b}\exp\left(\frac{E}{kT_m^2}(T - T_m)\right)\right]^{-\frac{b}{b-1}}$$

where I_m is the maximum intensity, T_m is the peak temperature, E is the activation energy, and b is the kinetic order parameter. This formulation enables the decomposition of complex TL glow curves into their constituent trapping components and allows estimation of the corresponding kinetic parameters [71]. The deconvolution analysis was performed using the tgcd software package developed for TL glow-curve analysis [72].

The CGCD results obtained at different irradiation doses (50, 75, 100, and 150 Gy) are presented in Fig. 8. For each dose, the experimental glow curve, fitted signal, and individual deconvoluted components are shown, together with the residuals. The overall fits exhibit low FOM values (~1.5–2.4%), indicating reliable decomposition across all irradiation conditions. These segments are used only as qualitative diagnostics of trap complexity and do not represent individually fitted TL peaks. The overall fit reproduces the measured TL signal with good agreement, yielding FOM values consistent with those obtained across different irradiation doses, further confirming the robustness of the deconvolution. The analysis reveals that the TL emission consists of thirteen partially overlapping glow peaks, distributed over the temperature range from approximately 65 °C to 470 °C. In particular, the positions and shapes of the deconvoluted peaks remain nearly unchanged across different doses, further confirming the robustness of the CGCD model.

The number of individual components used in the CGCD analysis was guided by the kinetic diagnostics obtained from the IR and T_m–T_{stop} analysis (Fig. 7**b**), which indicated a progressively evolving trap population rather than a single discrete trapping level. The presence of several quasi-stable E_a regions (P1–P12) suggests multiple overlapping trapping states contributing to the composite glow curve. The number of deconvolution components was increased progressively, starting from a small number of broad peaks, and additional components were introduced only when systematic structure remained in the residuals. This procedure avoids overfitting individual noise fluctuations and ensures that each added peak produces a statistically and physically justified improvement in the fit quality (FOM ≈ 1.5–2.4% across different irradiation doses). The kinetic parameters extracted from the CGCD analysis at different irradiation doses are summarized in Table 5. The parameters obtained for different doses show a high degree of consistency in activation energies, kinetic order, and frequency factors, confirming the stability and physical reliability of the deconvolution model. The activation energies increase systematically from approximately 0.87 eV for the first peak to about 1.98 eV for the higher-temperature components across all irradiation doses, demonstrating a consistent hierarchical trap structure with progressively increasing thermal stability. The corresponding peak temperatures shift from the low-temperature region (~65 °C) toward deeper traps appearing above ~350 °C and extending up to ~470 °C across all irradiation doses, which dominate the high-temperature part of the glow curve. No systematic variation of the activation energies, kinetic order, or frequency factors with increasing irradiation dose is observed, indicating that the trap structure and recombination kinetics are intrinsic properties of the material rather than dose-dependent effects.

The kinetic order parameter b obtained from the fits generally falls in the range 1.2–1.5, indicating that the dominant TL components follow general-order recombination kinetics rather than strictly first-order ($b = 1$) or second-order ($b = 2$) behavior, with significant retrapping contributions within a distributed trap system. This reflects the presence of significant retrapping processes and a complex recombination pathway involving multiple interacting traps. Therefore, the TL response of $GdBa_3B_9O_{18}$ is best described within a general-order kinetic framework governed by a distributed trap system. Although some of the VHR methods applied in this study were originally derived assuming first-order kinetics, their use follows standard practice in TL analysis as effective tools for estimating activation energies and frequency factors for such general-order systems.

The frequency factors ($s \approx 10^{11}$–10^{13} s^{-1}) obtained from the CGCD analysis should be interpreted as effective kinetic parameters associated with general-order peaks within a distributed trap hierarchy, rather than as descriptors of isolated, non-interacting traps. In such systems, simple lifetime estimates based on first-order kinetics ($\tau \approx s^{-1}\exp(E/kT)$) are not directly applicable, since charge carriers can undergo retrapping and redistribution among multiple trap levels prior to recombination. This behavior is consistent with the experimentally observed non-monotonic fading (anti-fading), which reflects time-dependent charge transfer from shallow to deeper traps, leading to an apparent extension of the macroscopic storage time. The estimated lifetimes (τ) of the individual TL components, calculated using this first-order approximation at room temperature, are summarized in Table 5(e) and should be regarded as indicative values for comparative purposes only. The extremely large τ values obtained for deeper traps are consistent with those commonly reported for high activation energies in TL materials. However, in systems exhibiting general-order kinetics and significant retrapping, such values should not be interpreted as actual storage lifetimes, but rather as indicative parameters reflecting the depth and thermal stability of traps within a distributed trap hierarchy.The progressive increase in activation energy derived from CGCD (0.87–1.98 eV) closely matches the E_a evolution observed in the IR–T_{stop} analysis (Fig. 7b) across all irradiation doses, providing strong evidence that the TL emission in $GdBa_3B_9O_{18}$ arises from a hierarchical and energetically distributed system of overlapping traps rather than a single isolated trapping level. The individual peaks obtained from the CGCD analysis should therefore be regarded as a discrete representation of an underlying distributed trap spectrum, rather than strictly independent physical trapping levels. Such an interpretation is consistent with previous studies on persistent phosphors, where broad TL glow curves and multiple fitted components were shown to originate from a continuous distribution of trap depths rather than isolated discrete trapping levels, further supporting the physical validity of the present CGCD analysis [40]. The calculated lifetimes are discussed separately in Table 5e as indicative parameters of trap stability.

Table 4. Kinetic parameters obtained from CGCD analysis of the TL glow curves of $GdBa_3B_9O_{18}$ at different irradiation doses: (a) 50 Gy, (b)

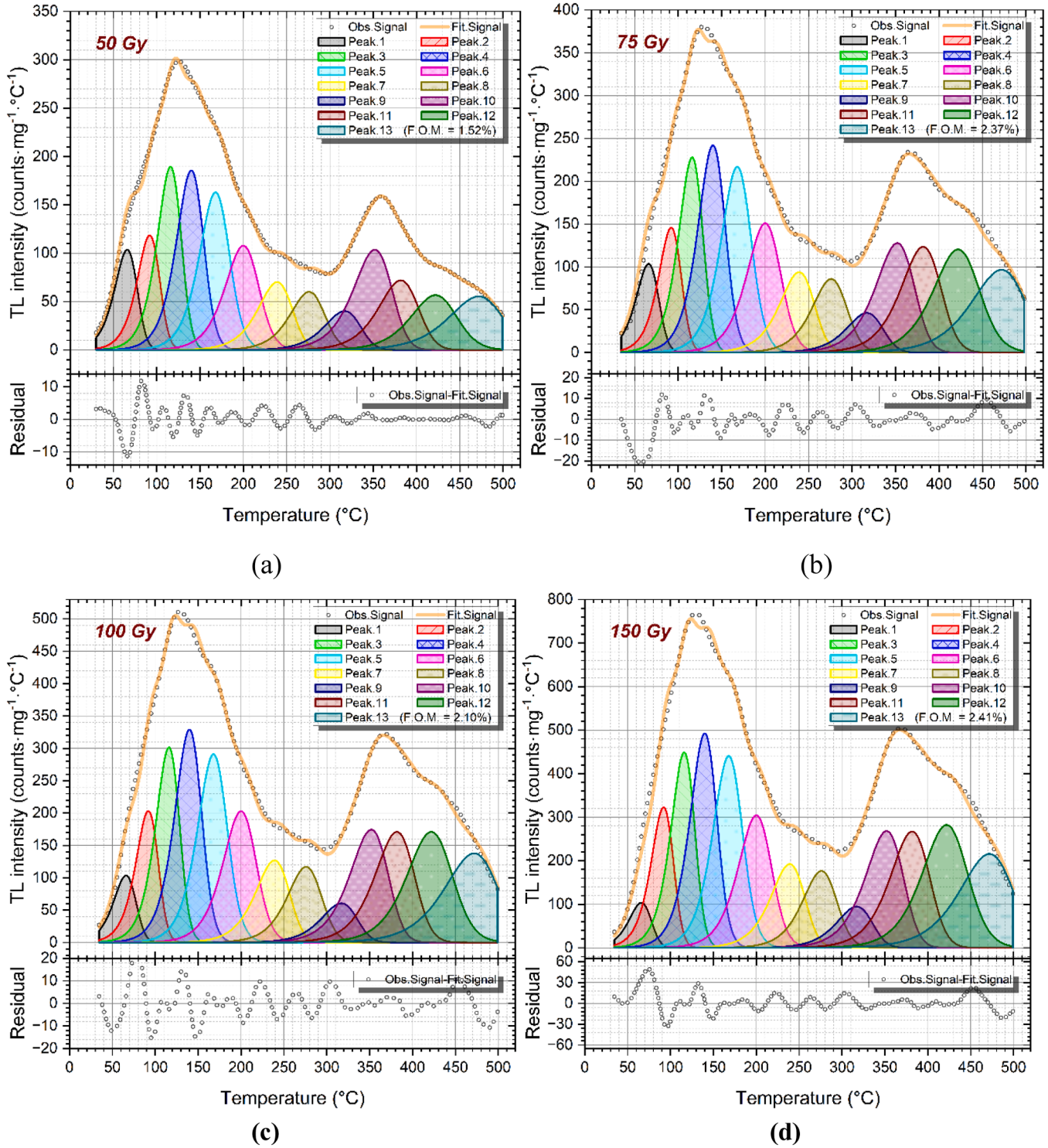

Fig. 8. Computerized glow curve deconvolution (CGCD) of the TL glow curves of $GdBa_3B_9O_{18}$ recorded at different irradiation doses (50, 75, 100, and 150 Gy). For each dose, the experimental signal (open symbols), fitted curve (solid line), and individual glow-peak components are shown. The lower panels present the residuals between the experimental and fitted signals. The consistent decomposition across different doses, with low figure-of-merit values (FOM ≈ 1.5–2.4%), demonstrates the reliability and stability of the extracted kinetic parameters.

75 Gy, (c) 100 Gy, and (d) 150 Gy, including activation energy (E_a), peak temperature (T_m), kinetic order (b), symmetry factor (μ), and frequency factor (*s*) for each deconvoluted component. (e) Estimated lifetimes (τ) of the corresponding TL components calculated at room temperature (300 K) using the first-order approximation $\tau = s^{-1}\exp(E/kT)$.

5. Fading behavior and time-dependent charge redistribution

The temporal stability of the TL signal in $GdBa_3B_9O_{18}$ was investigated by monitoring the evolution of the glow curves after different storage times following irradiation. The glow curves recorded after fading durations ranging from seconds to one day are presented in Fig. 9**a.** While the general structure of the glow curve remains preserved,

Table 5
Kinetic parameters obtained from CGCD analysis of the TL glow curves of $GdBa_3B_9O_{18}$ at different irradiation doses (a) 50, (b) 75, (c) 100, and (d)150 Gy), including activation energy (E_a), peak temperature (T_m), kinetic order (b), symmetry factor (μ), and frequency factor (s) for each deconvoluted component. (e) Estimated lifetimes (τ) of the corresponding TL components calculated at room temperature (300 K) using the first-order approximation $\tau = s^{-1}\exp E/kT$.

(a)

Dose(Gy)	Peaks	E_a (eV)	T_m (°C)	T_{m1} (°C)	T_{m2} (°C)	b	μ	s (s^{-1})
50 Gy	1st Peak	0.87	65.85	48.20	79.40	1.25	0.435	1.48×10^{12}
	2nd Peak	1.01	91.85	74.22	105.38	1.25	0.435	1.53×10^{13}
	3rd Peak	1.09	115.87	97.20	130.40	1.28	0.438	2.17×10^{13}
	4th Peak	1.13	139.85	119.17	156.57	1.37	0.447	9.25×10^{12}
	5th Peak	1.22	167.85	145.51	186.79	1.49	0.459	1.24×10^{13}
	6th Peak	1.22	199.97	174.59	220.91	1.42	0.455	1.22×10^{12}
	7th Peak	1.31	238.93	212.24	259.32	1.24	0.435	8.91×10^{11}
	8th Peak	1.55	275.85	249.37	296.99	1.34	0.444	1.98×10^{13}
	9th Peak	1.64	316.85	288.67	338.18	1.22	0.431	1.10×10^{13}
	10th Peak	1.74	351.85	321.92	374.71	1.24	0.433	1.09×10^{13}
	11th Peak	1.87	381.62	350.84	405.57	1.28	0.434	1.98×10^{13}
	12th Peak	1.98	421.85	387.73	450.67	1.48	0.458	2.60×10^{13}
	13th Peak	1.77	471.85	429.95	NA	1.25	NA	2.11×10^{10}

(b)

Dose(Gy)	Peaks	E_a (eV)	T_m (°C)	T_{m1} (°C)	T_{m2} (°C)	b	μ	s (s^{-1})
75 Gy	1st Peak	0.87	65.85	48.20	79.40	1.25	0.435	1.48×10^{12}
	2nd Peak	1.01	91.85	74.22	105.38	1.25	0.435	1.53×10^{13}
	3rd Peak	1.09	115.87	97.20	130.40	1.28	0.438	2.17×10^{13}
	4th Peak	1.13	139.85	119.17	156.57	1.37	0.447	9.25×10^{12}
	5th Peak	1.22	167.85	145.51	186.79	1.49	0.459	1.24×10^{13}
	6th Peak	1.22	199.97	174.59	220.91	1.42	0.455	1.22×10^{12}
	7th Peak	1.31	238.93	212.24	259.32	1.24	0.435	8.91×10^{11}
	8th Peak	1.55	275.85	249.37	296.99	1.34	0.444	1.98×10^{13}
	9th Peak	1.64	316.85	288.67	338.18	1.22	0.431	1.10×10^{13}
	10th Peak	1.74	351.85	321.92	374.71	1.24	0.433	1.09×10^{13}
	11th Peak	1.87	381.62	350.84	405.57	1.28	0.434	2.46×10^{13}
	12th Peak	1.98	421.85	387.73	450.67	1.48	0.458	2.11×10^{13}
	13th Peak	1.77	471.85	429.95	NA	1.25	NA	6.48×10^{10}

(c)

Dose(Gy)	Peaks	E_a (eV)	T_m (°C)	T_{m1} (°C)	T_{m2} (°C)	b	μ	s (s^{-1})
100 Gy	1st Peak	0.87	48.20	79.40	1.25	0.433	65.88	1.48×10^{12}
	2nd Peak	1.01	74.22	105.38	1.25	0.445	91.51	1.53×10^{13}
	3rd Peak	1.09	97.20	130.40	1.28	0.435	115.97	2.17×10^{13}
	4th Peak	1.13	119.16	156.58	1.37	0.463	139.27	9.25×10^{12}
	5th Peak	1.22	145.50	186.80	1.49	0.446	168.39	1.24×10^{13}
	6th Peak	1.22	174.59	220.91	1.42	0.455	199.84	1.22×10^{12}
	7th Peak	1.31	212.23	259.32	1.24	0.422	239.45	8.91×10^{11}
	8th Peak	1.55	249.37	296.99	1.34	0.450	275.56	1.98×10^{13}
	9th Peak	1.64	288.66	338.18	1.22	0.441	316.33	1.10×10^{13}
	10th Peak	1.74	321.91	374.72	1.24	0.444	351.27	1.09×10^{13}
	11th Peak	1.87	350.79	405.60	1.28	0.439	381.56	2.46×10^{13}
	12th Peak	1.98	387.72	450.67	1.48	0.450	422.33	2.11×10^{13}
	13th Peak	1.77	429.94	NA	1.25	NA	472.42	6.48×10^{10}

(d)

Dose(Gy)	Peaks	E_a (eV)	T_m (°C)	T_{m1} (°C)	T_{m2} (°C)	b	μ	s (s^{-1})
150 Gy	1st Peak	0.87	65.94	48.20	79.40	1.25	0.431	1.48×10^{12}
	2nd Peak	1.01	91.56	74.22	105.38	1.25	0.443	1.53×10^{13}
	3rd Peak	1.09	116.02	97.20	130.40	1.28	0.433	2.17×10^{13}
	4th Peak	1.13	139.32	119.16	156.57	1.37	0.461	9.25×10^{12}
	5th Peak	1.22	167.27	145.50	186.80	1.49	0.473	1.24×10^{13}
	6th Peak	1.22	199.88	174.59	220.91	1.42	0.454	1.22×10^{12}
	7th Peak	1.31	239.48	212.23	259.32	1.24	0.421	8.91×10^{11}
	8th Peak	1.55	275.59	249.37	296.99	1.34	0.449	1.98×10^{13}
	9th Peak	1.64	316.36	288.66	338.18	1.22	0.441	1.10×10^{13}
	10th Peak	1.74	351.30	321.91	374.72	1.24	0.443	1.09×10^{13}
	11th Peak	1.87	381.58	350.79	405.60	1.28	0.438	2.46×10^{13}
	12th Peak	1.98	422.35	387.72	450.67	1.48	0.450	2.11×10^{13}
	13th Peak	1.77	472.43	429.94	NA	1.25	NA	6.48×10^{10}

(e)

Peak index	**Equivalent Time**
Peak.1	~5.7 min
Peak.2	~2.15 h
Peak.3	~1.42 days
Peak.4	~15.8 days
Peak.5	~1.07 years
Peak.6	~10.9 years
Peak.7	~494.4 years
Peak.8	~254,500 years
Peak.9	~15.2 million years

(*continued on next page*)

Table 5 (*continued*)

Peak.10	~751 million years
Peak.11	~52.6 billion years
Peak.12	~4.44 trillion years
Peak.13	~386 billion years

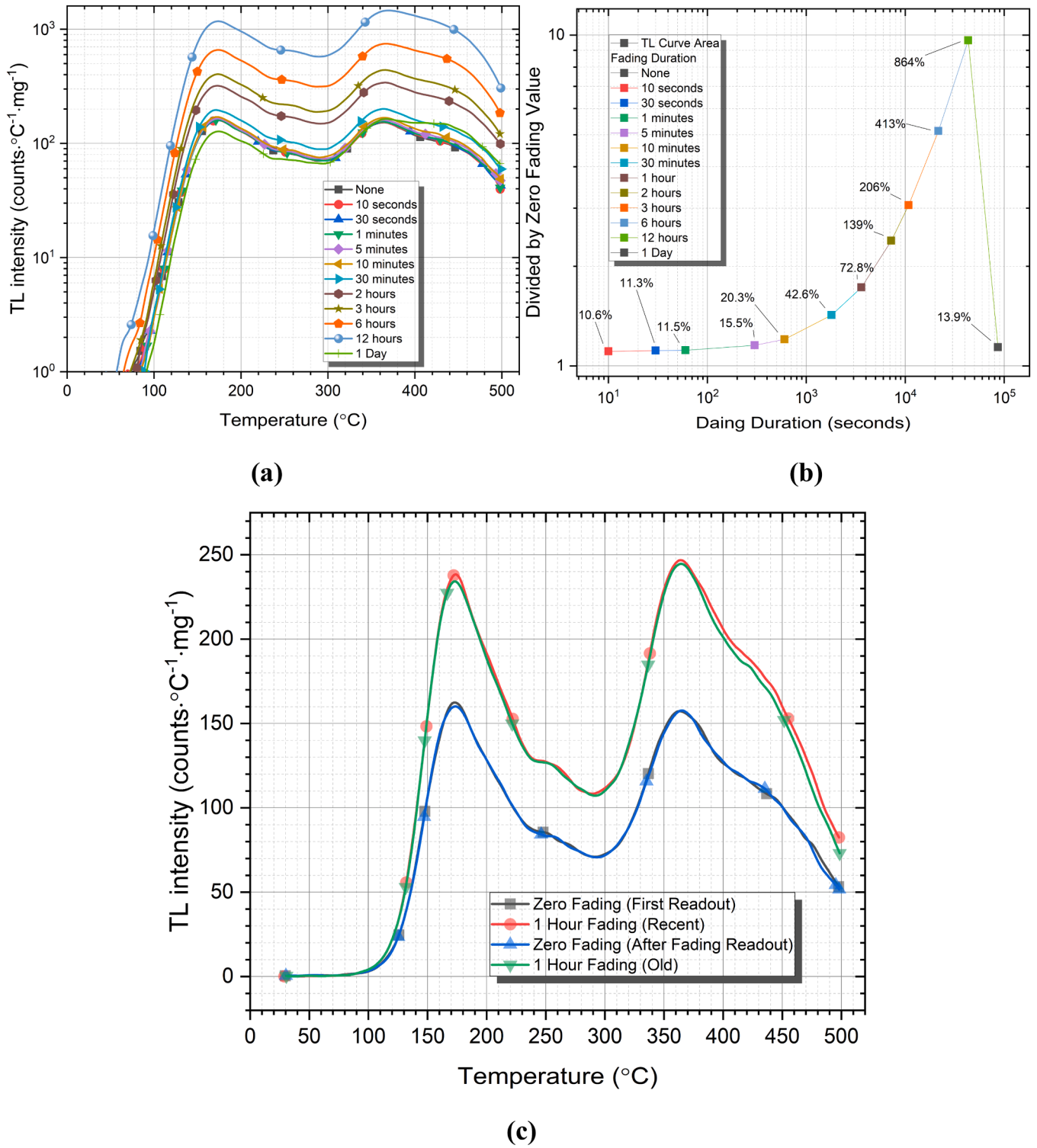

Fig. 9. (a) TL glow curves of $GdBa_3B_9O_{18}$ recorded after different fading durations ranging from seconds to one day. (b) Evolution of the normalized TL intensity of the dominant glow peak at ~172 °C as a function of fading duration. The dashed line (y = 1) represents the zero-fading reference level, while deviations from this level indicate anti-fading (increase) and conventional fading (decrease) behavior. (c) Comparison of TL glow curves before and after fading to verify the stability of the glow-curve shape and to assess possible effects on reusability.

the overall TL intensity exhibits a non-monotonic time evolution with storage time.

To quantify this behaviour, the integrated TL area was normalized to the initial readout value and plotted as a function of fading time (Fig. 9**b**). During the first several hours after irradiation, the TL intensity shows a gradual increase, reaching a maximum after approximately 12 h. This initial signal enhancement indicates an anti-fading behaviour rather than the conventional monotonic signal loss typically observed in TL materials. After longer storage times (≈1 day), a pronounced decrease in TL intensity is observed, marking the onset of conventional fading. This behaviour follows an initial anti-fading stage, during which the TL intensity increases instead of exhibiting the monotonic signal loss typically observed in TL materials. Extended measurements up to 20 days further confirm that this non-monotonic behaviour evolves into a long-term decay regime, consistent with the gradual thermal depopulation of traps and stabilization of the charge distribution.

Such two-stage temporal evolution can be understood in the framework of a hierarchical trap system with significant retrapping processes. In materials exhibiting distributed trap spectra, carriers released from relatively shallow trapping states may be retrapped into deeper and more radiatively efficient traps during the post-irradiation relaxation period, leading to a time-dependent redistribution of trapped charge carriers and a transient enhancement of the TL signal [28,40]. The presence of general-order recombination kinetics inferred from the CGCD analysis ($b \approx 1.2$–1.5) further supports the existence of substantial retrapping processes capable of redistributing charge among available trapping states.

After longer storage periods, the progressive decrease of the TL signal is most likely associated with the gradual loss of trapped carriers through thermally assisted escape from trapping states and subsequent recombination or tunnelling processes, leading to conventional fading. Once the redistribution processes approach equilibrium, thermal depopulation of traps becomes the dominant mechanism, resulting in the observed fading of the TL signal.

The fading behaviour is therefore consistent with the hierarchical trap structure inferred from the IR–T_{stop} diagnostics and the CGCD analysis, both of which indicated the presence of multiple overlapping traps spanning a broad activation-energy range (~0.8–2.0 eV). Within such a distributed trap landscape, time-dependent charge redistribution and retrapping can temporarily enhance the TL emission before eventual carrier loss leads to signal decay.

Finally, the comparison of glow curves before and after the fading experiment (Fig. 9**c**) confirms that the overall glow-curve structure remains stable, indicating that the fading process does not permanently modify the trapping–recombination framework of the material. This observation suggests that the observed signal variation originates primarily from reversible charge redistribution among trapping states rather than permanent structural modification of trapping centers, further supporting the distributed trap hierarchy revealed by the VHR, IR–T_{stop} and CGCD analyses. Although the observed anti-fading behavior is consistent with time-dependent charge redistribution and retrapping within a hierarchical trap system, direct identification of the specific retrapping pathways between trap groups cannot be established unambiguously from the present data and would require dedicated thermal bleaching experiments at selected preheat temperatures.

6. Conclusions

In this first thermoluminescence (TL) investigation of trigonal $GdBa_3B_9O_{18}$, X-ray diffraction analysis confirmed that the synthesized material crystallizes as a single-phase trigonal borate (space group $P6_3/m$), indicating the structural stability of the $GdBa_3B_9O_{18}$ phosphor. The phosphor exhibits a stable glow-curve shape with a near-linear dose response between 1.4 and 200 Gy and only mild supralinearity up to 500 Gy, together with a minimum detectable dose of ~0.11 Gy and reusability within ±5% over at least ten cycles, indicating its suitability for medium- to high-dose dosimetry in the Gy range.

All TL analyses were performed using the dominant emission channel at 410 nm, which represents the principal recombination pathway and provides a consistent basis for interpreting the trap-related TL processes. Heating-rate experiments combined with Kitis–Tuyn temperature-lag correction confirm that peak shifts are governed predominantly by intrinsic TL kinetics.

Multi-method kinetic analysis (VHR, IR–T_m–T_{stop}, CGCD) consistently reveals a hierarchical trap spectrum spanning ~0.87–1.98 eV with general-order recombination kinetics ($b \approx 1.2$–1.5), indicating an energetically distributed trap hierarchy. Within this framework, fading measurements reveal an initial anti-fading stage in which the TL intensity increases during the first ~12 h after irradiation before the onset of conventional signal decay. Extended fading measurements up to 20 days further confirm that this non-monotonic behavior evolves into a long-term decay regime. This behavior is consistent with time-dependent charge redistribution among traps in a hierarchical trapping system and further supports the distributed trap structure governing the TL response.

Finally, the combined IR–T_m–T_{stop}, VHR, and CGCD analyses demonstrate that the trapping centers in $GdBa_3B_9O_{18}$ follow general-order recombination kinetics ($b \approx 1.2$–1.5) within a hierarchical and energetically distributed trap spectrum ($E_a \approx 0.87$–1.98 eV).

Within this framework, the frequency factors on the order of 10^{11}–10^{13} s^{-1} obtained for the dominant TL components should be interpreted as effective kinetic parameters of overlapping traps rather than as descriptors of isolated levels. Consequently, simple first-order lifetime estimates are not applicable, and the observed TL stability, including the initial ~12 h anti-fading behavior followed by conventional decay, is consistent with retrapping and time-dependent charge redistribution within the trap hierarchy. While the present results are consistent with a retrapping-driven redistribution mechanism, a quantitative identification of individual trap-to-trap transfer pathways remains beyond the scope of the current study.

CRediT authorship contribution statement

Jabir Hakami: Methodology, Investigation, Conceptualization. **Abeer S. Altowyan:** Writing – original draft, Methodology, Investigation, Funding acquisition, Formal analysis. **Cin E. A.:** Methodology, Investigation, Formal analysis. **M. Oglakci:** Methodology, Investigation, Formal analysis. **M.B. Coban:** Software, Methodology, Investigation, Funding acquisition. **U.H. Kaynar:** Software, Methodology, Investigation. **Can Nurdogan:** Writing – review & editing, Writing – original draft, Conceptualization.

Declaration of Competing Interest

The authors declare that they have no known competing financial interests or personal relationships that could have appeared to influence the work reported in this paper.

Acknowledgements

The authors acknowledge the Princess Nourah bint Abdulrahman University Researchers Supporting Project (Project No. PNURSP2026R16), Princess Nourah bint Abdulrahman University, Riyadh, Saudi Arabia. We would like to express our sincere gratitude to the Research Funds of Balikesir University (Grant No. BAP-2026/018) for the financial support.

References

[1] M. Bakr, M. Omer, Determination of thermoluminescence kinetic parameters of La_2O_3 doped with Dy^{3+} and Eu^{3+}, Materials 13 (2020) 1047, https://doi.org/10.3390/ma13051047.

[2] B.A. Kumar, P.H. Bindu, Advances in borate- and phosphate-based TL materials for in vivo dosimetry, J. Korean Ceram. Soc. 59 (2022) 537–550, https://doi.org/10.1007/s43207-022-00240-x.

[3] A.Y. Madkhli, D.A. Jabali, G. Souadi, M. Sonsuz, U.H. Kaynar, S. Akça-Özalp, M. Ayvacikli, O. Madkhali, M. Topaksu, N. Can, Beta irradiation-induced thermoluminescence: glow curve analysis and kinetic parameters in combustion-synthesized undoped $Ca_4YO(BO_3)_3$, Appl. Radiat. Isot. 208 (2024) 111301, https://doi.org/10.1016/j.apradiso.2024.111301.

[4] D.A. Naprasnikov, V.V. Maltsev, N.I. Leonyuk, $YAl_3(BO_3)_4$- and $GdAl_3(BO_3)_4$-based glass-ceramic composites, Inorg. Mater. 52 (2016) 68–75, https://doi.org/10.1134/S0020168515120092.

[5] S.S. Rojas, K. Yukimitu, A.S.S. de Camargo, L.A.O. Nunes, A.C. Hernandes, Undoped and calcium doped borate glass system for thermoluminescent dosimeter, J. Non Cryst. Solids 352 (2006) 3608–3612, https://doi.org/10.1016/j.jnoncrysol.2006.02.128.

[6] B. Malysa, A. Meijerink, T. Jüstel, Temperature dependent luminescence Cr^{3+}-doped $GdAl_3(BO_3)_4$ and $YAl_3(BO_3)_4$, J. Lumin 171 (2016) 246–253, https://doi.org/10.1016/j.jlumin.2015.10.042.

[7] L.V. da, S. França, Development and characterization of new borate-based compounds for X-rays, gamma rays and neutron luminescence dosimetry, Univ. De. São Paulo (2022), https://doi.org/10.11606/T.59.2022.tde-04102023-065627.

[8] L.V.S. França, E. Müller, E.G. Yukihara, O. Baffa, A Tb and Ag co-doped borate compound forms a high sensitive X-ray, gamma-ray and neutron luminescence dosimeter, J. Mater. Chem. C. 11 (2023) 4444–4455, https://doi.org/10.1039/D3TC00223C.

[9] A. Alshoaibi, P.O. Ike, C. Awada, E.O. Echeweozo, S. Islam, F.I. Ezema, Gadolinium doped lithium aluminum borate $[Li_3Al_3(BO_3)_4$:Gd] materials synthesized and characterized for its structural, optical and thermoluminescence properties for use in dosimetric application, Radiat. Phys. Chem. 229 (2025) 112445, https://doi.org/10.1016/j.radphyschem.2024.112445.

[10] M.J. Knitel, P. Dorenbos, C.W.E. van Eijk, B. Plasteig, B. Viana, A. Kahn-Harari, D. Vivien, Photoluminescence, and scintillation/thermoluminescence yields of several Ce^{3+} and Eu^{2+} activated borates, Nucl. Instrum. Methods Phys. Res. Sect. A Accel. Spectrometers Detect. Assoc. Equip. 443 (2000) 364–374, https://doi.org/10.1016/S0168-9002(99)01154-7.

[11] Y. Alajlani, M. Sonsuz, A. Barad, Ü.H. Kaynar, M. Ayvacikli, M. Topaksu, N. Can, Thermoluminescence in $GdAl_3(BO_3)_4$ phosphors: Unusual heating rate dependencies, dose responses and kinetic parameters, Appl. Radiat. Isot. 198 (2023) 110851, https://doi.org/10.1016/j.apradiso.2023.110851.

[12] Z.G. Portakal Uçar, Thermoluminescence characteristics and kinetic analysis of beta irradiated $Ca_4LaO(BO_3)3$ phosphor, Cumhur. Sci. J. 42 (2021) 702–714, https://doi.org/10.17776/csj.929279.

[13] G. Souadi, U.H. Kaynar, M. Oglakci, M. Sonsuz, M. Ayvacikli, M. Topaksu, A. Canimoglu, N. Can, Thermoluminescence characteristics of a novel Li_2MoO_4 phosphor: Heating rate, dose response and kinetic parameters, Radiat. Phys. Chem. 194 (2022) 110025, https://doi.org/10.1016/j.radphyschem.2022.110025.

[14] G. Souadi, Ü.H. Kaynar, M. Sonsuz, S. Akça-Özalp, M. Ayvacikli, M. Topaksu, O. T. Ozmen, N. Can, Unravelling the impact of unusual heating rate, dose-response and trap parameters on the thermoluminescence of Sm^{3+} activated $GdAl_3(BO_3)_4$ phosphors exposed to beta particle irradiation, Radiat. Phys. Chem. 213 (2023) 111211, https://doi.org/10.1016/j.radphyschem.2023.111211.

[15] Ü.H. Kaynar, M. Oglakci, K. Bulcar, S. Benourdja, M. Bakr, M. Ayvacikli, A. Canimoglu, M. Topaksu, N. Can, Comparison of thermoluminescence characteristics of undoped and europium doped $YAl_3(BO_3)_4$ phosphor synthesized by combustion method: Anomalous heating rate, dose response and kinetic analyses, Radiat. Phys. Chem. 204 (2023) 110657, https://doi.org/10.1016/j.radphyschem.2022.110657.

[16] D. Nolasco-Altamirano, A. Alonso-Sotolongo, J.F. Benavente-Cuevas, R. García-Salcedo, O.A. García-Gardunño, J. Zarate-Medina, V. Correcher, T. Rivera-Montalvo, Kinetic Parameters Analysis of $GdAlO_3$ Based on Thermoluminescent Phenomenon, Phys. Status Solidi 262 (2025), https://doi.org/10.1002/pssb.202400381.

[17] A. Abdelmonem, H.A. Alazab, E. Salama, Thermoluminescence glow curve deconvolution and kinetic parameter determination of samarium-doped lithium borosilicate glass, Luminescence 37 (2022) 302–309, https://doi.org/10.1002/bio.4172.

[18] S.A. Islam, M. Kamruzzaman, M.R. Rahat, S. Hossain, H.A. Abdul-Rashid, M. U. Khandaker, D.A. Bradley, M. Al-Mamun, A.K.M.M. Rahman, $LiZnBO_3$ phosphor for dosimetry applications, Radiat. Phys. Chem. 218 (2024) 111596, https://doi.org/10.1016/j.radphyschem.2024.111596.

[19] G.C. Del Rosario, E. Cruz-Zaragoza, M.G. Hipólito, J. Marcazzó, J.M. Hernández A, H. Murrieta S, Synthesis and stimulated luminescence property of $Zn(BO_2)_2$:Tb^{3+}, Appl. Radiat. Isot. 127 (2017) 103–108, https://doi.org/10.1016/j.apradiso.2017.05.018.

[20] O. Legorreta-Alba, E. Cruz-Zaragoza, D. Díaz, J. Marcazzó, Synthesis of MgB_4O_7:Dy^{3+} and Thermoluminescent Characteristics at Low Doses of Beta Radiation, J. Nucl. Phys. Mater. Sci. Radiat. Appl. 6 (2018) 71–76, https://doi.org/10.15415/jnp.2018.61012.

[21] A.S. Altowyan, M. Sonsuz, U.H. Kaynar, J. Hakami, Z.G. Portakal-Uçar, M. Ayvacikli, M. Topaksu, N. Can, Synthesis and thermoluminescence behavior of novel Sm^{3+} doped $YCa_4O(BO_3)_3$ under beta irradiation, Ceram. Int. 50 (2024) 19681–19691, https://doi.org/10.1016/j.ceramint.2024.03.089.

[22] B. Ullah, M.B. Kakakhel, S. Ur Rehman, M.T. Siddique, M. Munir, K. Ahmad, M. M. Mahmood, M. Wazir-ud-Din, I. Anjum, Synthesis and dosimetric characterization of lithium tetraborate ($Li_2B_4O_7$:Cu,Ag) thermoluminescent dosimeter with improved reproducibility and reusability, Radiat. Phys. Chem. 220 (2024) 111704, https://doi.org/10.1016/j.radphyschem.2024.111704.

[23] R. Nattudurai, L. Sangeetha, K. Sivaraj, P. Kokila, New thermoluminescence dosimetric characteristics of Cu-doped $Li_2B_4O_7$ phosphors with X-rays, gamma, and proton beams, J. Mater. Sci. Mater. Electron 35 (2024) 2240, https://doi.org/10.1007/s10854-024-14015-z.

[24] H. Toktamis, T.S. Güneş, D. Toktamis, Investigation of the Use of Naturally Grown $CaCO_3$ Crystals on Rocks as a Radiation Dosimeter via Thermoluminescence Method, Luminescence 40 (2025), https://doi.org/10.1002/bio.70217.

[25] J. Peng, G. Kitis, A.M. Sadek, E.C. Karsu Asal, Z. Li, Thermoluminescence glow-curve deconvolution using analytical expressions: A unified presentation, Appl. Radiat. Isot. 168 (2021) 109440, https://doi.org/10.1016/j.apradiso.2020.109440.

[26] T.S. Sarkar, S. Sarkar, S. Bhattacharyya, P.S. Majumdar, A Study toward the Model Independence of Various Heating Rates Method in Thermoluminescence Glow Curve Analysis, Phys. Status Solidi 261 (2024), https://doi.org/10.1002/pssb.202400157.

[27] H.J. Alathlawi, A. Barad, O. Madkhali, G. Souadi, M. Sharahili, J. Hakami, S. Balci, U.H. Kaynar, M. Topaksu, N. Can, Intrinsic thermoluminescence and anomalous heating rate effects in undoped $K_7SrY_2(B_5O_{10})_3$ Phosphors: A combined Tm–Tstop and GOK deconvolution study, Appl. Radiat. Isot. 225 (2025) 112092, https://doi.org/10.1016/j.apradiso.2025.112092.

[28] J.F. Benavente, J.M. Gómez-Ros, V. Correcher, Characterization of the thermoluminescence glow curve of $Li_2B_4O_7$:Cu,Ag, Radiat. Meas. 137 (2020) 106427, https://doi.org/10.1016/j.radmeas.2020.106427.

[29] P.P. Kulkarni, K.H. Gavhane, M.S. Bhadane, V.N. Bhoraskar, S.S. Dahiwale, S. D. Dhole, Investigation of the photoluminescence and novel thermoluminescence dosimetric properties of $NaGdF_4$:Tb^{3+} phosphors, Mater. Adv. 1 (2020) 1113–1124, https://doi.org/10.1039/D0MA00247J.

[30] J.-G. Li, Y. Sakka, Recent progress in advanced optical materials based on gadolinium aluminate garnet ($Gd_3Al_5O_{12}$), Sci. Technol. Adv. Mater. 16 (2015) 014902, https://doi.org/10.1088/1468-6996/16/1/014902.

[31] J. Li, J.-G. Li, J. Li, S. Liu, X. Li, X. Sun, Y. Sakka, Development of Eu^{3+} activated monoclinic, perovskite, and garnet compounds in the Gd_2O_3–Al_2O_3 phase diagram as efficient red-emitting phosphors, J. Solid State Chem. 206 (2013) 104–112, https://doi.org/10.1016/j.jssc.2013.08.003.

[32] E. Hertle, L. Chepyga, A. Osvet, C.J. Brabec, M. Batentschuk, S. Will, L. Zigan, Gd, Lu)AlO_3:Dy^{3+} and (Gd,Lu)$_3Al_5O_{12}$:Dy^{3+} as high-temperature thermographic phosphors, Meas. Sci. Technol. 30 (2019) 034001, https://doi.org/10.1088/1361-6501/aafcac.

[33] M. Oglakci, M. Topaksu, G. Souadi, N. Can, Thermoluminescence study and trapping parameters of beta irradiated $NaBaBO_3$:Gd^{3+} phosphor, J. Lumin 238 (2021) 118245, https://doi.org/10.1016/j.jlumin.2021.118245.

[34] K. Bulcar, M. Oglakci, U.H. Kaynar, M. Ayvacikli, G. Souadi, M. Topaksu, N. Can, Thermoluminescence glow curve analysis and evaluation of trapping parameters of dysprosium doped lanthanum calcium borate $La_2CaB_{10}O_{19}$, Nucl. Instrum. Methods Phys. Res. Sect. B Beam Interact. Mater. At. 489 (2021) 58–68, https://doi.org/10.1016/j.nimb.2020.12.023.

[35] S. Nabadwip Singh, Analysis of the thermoluminescent of borate glass by computerized glow curve deconvolution in kinetic formalism, J. Phys. Conf. Ser. 2070 (2021) 012009, https://doi.org/10.1088/1742-6596/2070/1/012009.

[36] D. Richter, A. Richter, K. Dornich, Lexsyg smart — a luminescence detection system for dosimetry, material research and dating application, Geochronometria 42 (2015) 202–209, https://doi.org/10.1515/geochr-2015-0022.

[37] X.Z. Li, C. Wang, X.L. Chen, H. Li, L.S. Jia, L. Wu, Y.X. Du, Y.P. Xu, Syntheses, thermal stability, and structure determination of the novel isostructural $RBa_3B_9O_{18}$ (R = Y, Pr, Nd, Sm, Eu, Gd, Tb, Dy, Ho, Er, Tm, Yb), Inorg. Chem. 43 (2004) 8555–8560, https://doi.org/10.1021/ic049710m.

[38] M. Bakr, Z.G. Portakal-Uçar, M. Yüksel, Ü.H. Kaynar, M. Ayvacikli, S. Benourdja, A. Canimoglu, M. Topaksu, A. Hammoudeh, N. Can, Thermoluminescence properties of beta particle irradiated $Ca_3Al_2O_6$ phosphor relative to environmental dosimetry, J. Lumin 227 (2020) 117565, https://doi.org/10.1016/j.jlumin.2020.117565.

[39] S. Atasöz, M. Topaksu, G. Souadi, N. Can, Anomalous heating rate dependence and analyses of thermoluminescence glow curves in Gd doped ZnB_2O_4 phosphors, J. Lumin 246 (2022) 118838, https://doi.org/10.1016/j.jlumin.2022.118838.

[40] K. Van den Eeckhout, A.J.J. Bos, D. Poelman, P.F. Smet, Revealing trap depth distributions in persistent phosphors, Phys. Rev. B 87 (2013) 045126, https://doi.org/10.1103/PhysRevB.87.045126.

[41] D.J. Daniel, I.R. Panday, H.J. Kim, S. Kim, U. Fawad, Luminescence and low temperature trap centers in mixed rare earth borate crystal, J. Rare Earths 36 (2018) 1024–1029, https://doi.org/10.1016/j.jre.2018.02.011.

[42] D.J. Daniel, H.J. Kim, S. Kim, S. Kothan, J. Kaewkhao, Trap level analysis of Ce^{3+} and Sm^{3+} in $Li_6Y(BO_3)_3$, Ceram. Int. 45 (2019) 11893–11898, https://doi.org/10.1016/j.ceramint.2019.03.072.

[43] G.S. Polymeris, S. Çoskun, E. Tsoutsoumanos, P. Konstantinidis, E. Aşlar, E. Şahiner, N. Meriç, G. Kitis, Dose response features of quenched and reconstructed, TL and deconvolved OSL signals in BeO, Results Phys. 25 (2021) 104222, https://doi.org/10.1016/j.rinp.2021.104222.

[44] S.V. Nikiforov, V. Pagonis, A.S. Merezhnikov, Sublinear dose dependence of thermoluminescence as a result of competition between electron and hole trapping centers, Radiat. Meas. 105 (2017) 54–61, https://doi.org/10.1016/j.radmeas.2017.08.003.

[45] V. Pagonis, R. Chen, J.L. Lawless, Superlinear dose response of thermoluminescence (TL) and optically stimulated luminescence (OSL) signals in

luminescence materials: an analytical approach, J. Lumin 132 (2012) 1446–1455, https://doi.org/10.1016/j.jlumin.2012.01.014.
[46] R. Chen, S.W.S. McKeever, Theory of Thermoluminescence and Related Phenomena, World Scientific, 2011.
[47] V. Pagonis, G. Kitis, C. Furetta, Numerical and Practical Exercises in Thermoluminescence, Springer New York, New York, NY, 2006, https://doi.org/10.1007/0-387-30090-2.
[48] K. Burke, D. Sutton, Optimization and deconvolution of lithium fluoride TLD-100 in diagnostic radiology, Br. J. Radio. 70 (1997) 261–271, https://doi.org/10.1259/bjr.70.831.9166051.
[49] L.F. Souza, A.L.F. Novais, P.L. Antonio, L.V.E. Caldas, D.N. Souza, Luminescent properties of MgB_4O_7:Ce,Li to be applied in radiation dosimetry, Radiat. Phys. Chem. 164 (2019) 108353, https://doi.org/10.1016/j.radphyschem.2019.108353.
[50] M. Ehab, E. Salama, L.S. El-Ahll, H.A. Saudi, H.A.A. Ghany, H.A. Alazab, Preparation and thermoluminescence characteristics of ytterbium borosilicate glasses for radiation dosimetry applications, Luminescence 40 (2025), https://doi.org/10.1002/bio.70237.
[51] M. Panda, S. Chivukula, S. Joshi, M.G. Komathi, O. Annalakshmi, V.S. C, SMD chip resistors as reliable thermoluminescent dosimeters: dosimetric characterization and TL kinetics study, J. Lumin 280 (2025) 121094, https://doi.org/10.1016/j.jlumin.2025.121094.
[52] C. Le Deroff, E.A. Pérès, X. Ledoux, J. Toutain, A. Frelin-Labalme, vivo surface dosimetry with a scintillating fiber dosimeter in preclinical image-guided radiotherapy, Med. Phys. 47 (2020) 234–241, https://doi.org/10.1002/mp.13903.
[53] N. Esplen, L. Egoriti, T. Planche, S. Rädel, H.-W. Koay, B. Humphries, X. Ren, N. Ford, C. Hoehr, A. Gottberg, M. Bazalova-Carter, Dosimetric characterization of a novel UHDR megavoltage X-ray source for FLASH radiobiological experiments, Sci. Rep. 14 (2024) 822, https://doi.org/10.1038/s41598-023-50412-w.
[54] S.W.S. McKeever, Thermoluminescence of Solids, Cambridge University Press, 1985, https://doi.org/10.1017/CBO9780511564994.
[55] V. Pagonis, P. Morthekai, G. Kitis, Kinetic analysis of thermoluminescence glow curves in feldspar: evidence for a continuous distribution of energies, Geochronometria 41 (2014) 168–177, https://doi.org/10.2478/s13386-013-0148-z.
[56] A. Mandowski, The Theory of Thermoluminescence with an Arbitrary Spatial Distribution of Traps, Radiat. Prot. Dosim. 100 (2002) 115–118, https://doi.org/10.1093/oxfordjournals.rpd.a005825.
[57] A.J.J. Bos, Theory of thermoluminescence, Radiat. Meas. 41 (2006) S45–S56, https://doi.org/10.1016/j.radmeas.2007.01.003.
[58] G. Kitis, J.W.N. Tuyn, A simple method to correct for the temperature lag in TL glow-curve measurements, J. Phys. D. Appl. Phys. 31 (1998) 2065–2073, https://doi.org/10.1088/0022-3727/31/16/017.
[59] W. Hoogenstraaten, 1958, Electron Traps in Zinc-sulphide Phosphors, Faculteit der Wis- en Natuurkunde Universiteit van Amsterdam.
[60] W. Hoogenstraaten, Electron traps in zinc-sulphide phosphors, Philips Res. Rep. 13 (1958) 515–693.
[61] M.S. Rasheedy, Method of Hoogenstraaten as a tool for obtaining the trap parameters of general-order thermoluminescence glow peaks, Radiat. Eff. Defects Solids 160 (2005) 383–390, https://doi.org/10.1080/10420150500459999.
[62] A.H. Booth, Calculation of electron trap depths from thermoluminescence maxima, Can. J. Chem. 32 (1954) 214–215, https://doi.org/10.1139/v54-027.
[63] A. Bohun, Thermoemission und Photoemission von Natriumchlorid, Czechoslov. J. Phys. 4 (1954) 91–93, https://doi.org/10.1007/BF01688114.
[64] I.A. Parfianovitch, The determination of the depth of electron traps in crystal phosphors, J. Exp. Theor. Phys. 26 (1954) 696.
[65] M.S. Rasheedy, A.I. Abd-Elmageed, The validity of the two heating rates method to obtain the trapping parameters from general-order thermoluminescence glow peaks, J. Phys. Chem. Solids 68 (2007) 243–248, https://doi.org/10.1016/j.jpcs.2006.11.002.
[66] G. Souadi, K. Bulcar, A. Yucel, M. Oglakci, S. Sezer, O. Madkhali, T. Depci, M. Topaksu, N. Can, Radiation-induced thermoluminescence in $Ca_5(PO_4)_3OH$ powder from eggshell: Trapping parameter assessment, Radiat. Phys. Chem. 217 (2024) 111488, https://doi.org/10.1016/j.radphyschem.2023.111488.
[67] R.K. Gartia, S. Ingotombi, T.S.S. Sing, P.S. Mazumdar, On the determination of the activation energy of a thermoluminescence peak by the two-heating-rates method, J. Phys. D. Appl. Phys. 24 (1991) 65–69, https://doi.org/10.1088/0022-3727/24/1/011.
[68] S.W.S. McKeever, On the analysis of complex thermoluminescence. Glow-curves: resolution into individual peaks, Phys. Status Solidi 62 (1980) 331–340, https://doi.org/10.1002/pssa.2210620139.
[69] S. Balci-Yegen, C. Boronat, J. Garcia-Guinea, M. Topaksu, V. Correcher, Correlation between thermoluminescence emission and phase transitions of tridymite, Phase Transit. 91 (2018) 1122–1128, https://doi.org/10.1080/01411594.2018.1515435.
[70] M. Wazir-ud-Din, Shakeel-ur-Rehman, D. Poelman, J. De Grave, D. Vandenberghe, M. Basim Kakakhel, S. Hayat, N. Karimi Moayed, Thermoluminescence dosimetric and kinetic characterization of Pakistani fluorite after β irradiation, Nucl. Instrum. Methods Phys. Res. Sect. B Beam Interact. Mater. At. 540 (2023) 246–258, https://doi.org/10.1016/j.nimb.2023.04.031.
[71] J. M. G mez Ros, G. Kitis, Computerised glow curve deconvolution using general and mixed order kinetics, Radiat. Prot. Dosim. 101 (2002) 47–52, https://doi.org/10.1093/oxfordjournals.rpd.a006029.
[72] J. Peng, Z. Dong, F. Han, tgcd: an R package for analyzing thermoluminescence glow curves, SoftwareX 5 (2016) 112–120, https://doi.org/10.1016/j.softx.2016.06.001.